Magnetic and Electronic Properties of Ce doped Si Films

Magnetic and Electronic Properties of Ce doped Si Films

Daisuke Shindo

February 2011

Doctoral Thesis at Osaka Prefecture University

Contents

5　Heavily doping of Ce atom into Si

6　Summary

1

General Introduction

1.1   Background

Spintronics,[1,2] which is an interdisciplinary field including semiconductor electronics, magnetism, optics and related disciplines, provides great potential for next-generation devices capable of high-speed information processing and low power consumption. In recent years diluted magnetic semiconductors (DMSs), which are semiconductors doped with a magnetic impurity, have been intensively investigated because of their promise as materials for semiconductor-based spintronic devices. Although ferromagnetic DMSs based on III-V and II-VI compound semiconductors such as (In,Mn)As,[3,4] (Ga,Mn)As[5-7] and (Zn,Cr)Te[8,9] have been widely studied, ferromagnetic DMSs that are compatible with current Si integrated circuit technology are strongly needed. In particular, Si- and Ge-based ferromagnetic DMSs are attractive for integrated spintronics based on Si technology, and in recent years, group IV DMSs such as transition metal (TM)-doped Ge[10-13] and Si[14,15] have been studied.

We have been interested in a rare-earth (RE) element doped Si-based DMS. In this study, Ce which has one $4f$ electron was selected as a magnetic ion for a Si-based DMS. As shown in Figure 1-1, since $4f$ electrons of rare earth elements are screened by the outer shell electrons ($5s$, $5p$, and $6s$), they are strongly localized. However, Ce is different from other rare earth elements in the sense that the $4f$ shell is relatively

expanded and the wave function is broader than that of other rare earth elements. This nature of the $4f$ shell facilitates hybridization between Ce $4f$ spin and conduction electrons, and partial delocalization of the single $4f$ electron can occur [16-18]. Actually, there are two possible ground states of Ce $4f$ electron depending on the ligand of crystal field or element. One is trivalent state, which possesses magnetic ground state, and the other is tetravalent. Figure 1-2 shows the electron configuration of Ce trivalent (a) and tetravalent (b). The state of the $4f$ electron is important in Si:Ce DMS.
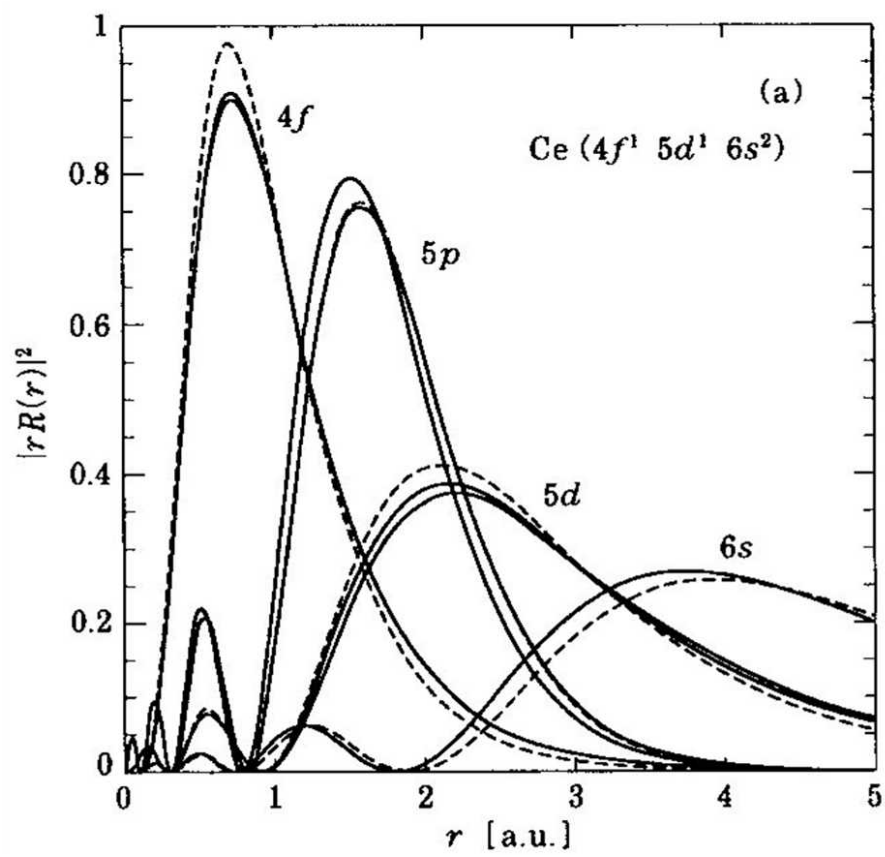
Fig.1-1. Radial wave function of Ce atom. K. Ueda and Y. Ohnuki: *Physics of heavy-fermion system* (Shokabo, 1998)p.11[in Japanese].

(a)

Ce^{3+} [Xe] $4f^1 5d^1 6s^2$

4s   4p   4d   4f

5s   5p   5d   5f

6s

(b)

Ce^{4+} [Xe] $4f^0 5d^2 6s^2$
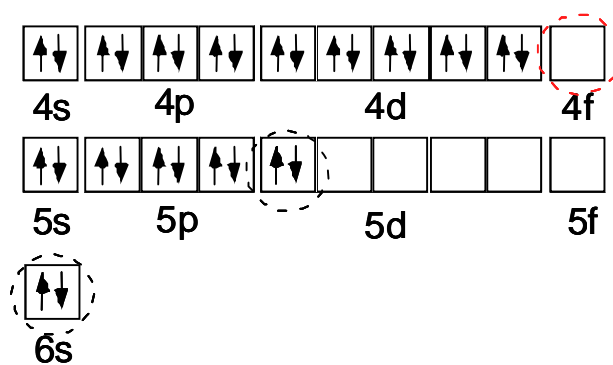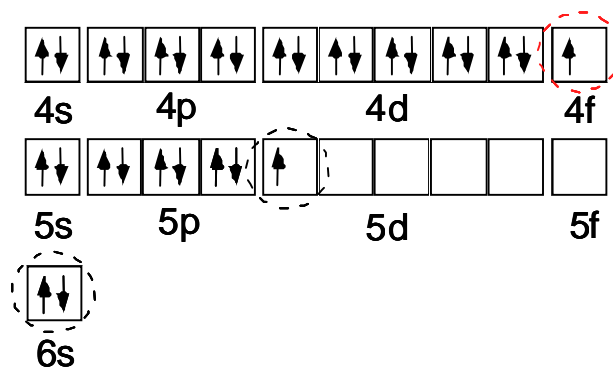

4s   4p   4d   4f

5s   5p   5d   5f

6s

Fig. 1-2.   Electron configuration of Ce trivalent (a) and tetravalent (b)

So far, various phenomena have been observed in Ce-doped Si. In Si:Ce bulk samples, antiferromagnetism, heavy fermion-type transport behavior, or ferromagnetic ordering has been observed [19]. The vacuum-evaporated Si:Ce films have been also prepared and various phenomena, such as ferromagnetic ordering, anomalous ρ-T behavior, spinglass behavior and/or giant magneto-resistance, have been observed [20,21]. Then, the MBE-grown Si:Ce films have also shown anomalous ρ-T and χ-T behavior, ferromagnetic ordering, and giant magneto-resistance [22,23].

1.2   Ce-doped Si

Let us take a look at the typical structural, magnetic, and magneto-transport properties of MBE-grown Si:Ce films. Figure 1-3 shows the XRD pattern (a), RHEED pattern (b), and surface morphology by AFM (c) of Si:0.5 at.%Ce film grown at 740 °C on Si(001) substrate by solid source MBE. The film thickness is 480 nm. The extra diffraction corresponding to CeSi$_x$ is not identified in XRD. No silicide precipitations were also recognized by the TED analysis. The RHEED pattern exhibits spotty streak without extra spots corresponding to precipitations, indicating that the film is grown epitaxially on Si(001) substrate. However, the large hillock formation is recognized in the AFM image. The films grown at 740 °C do not have smooth surfaces because of high growth temperature. Figure 1-4 shows the magnetization curve of this film measured at 2 K by SQUID. A positive magnetization and abrupt increase of magnetization at low magnetic field is observed. The magnetic susceptibility of the
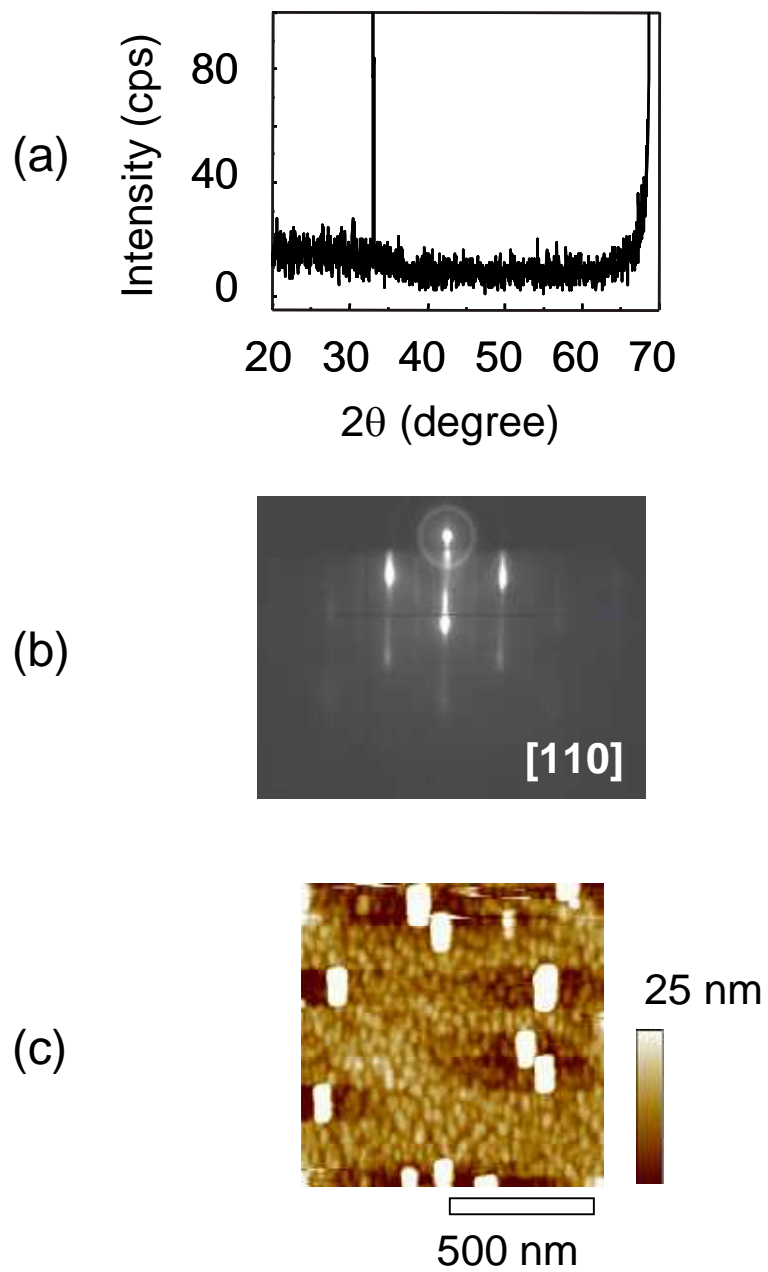
Fig. 1-3.   XRD pattern (a), RHEED pattern (b), and AFM image (c) of Si:0.5 at.% Ce film grown at 740 °C. The film thickness is 480 nm.
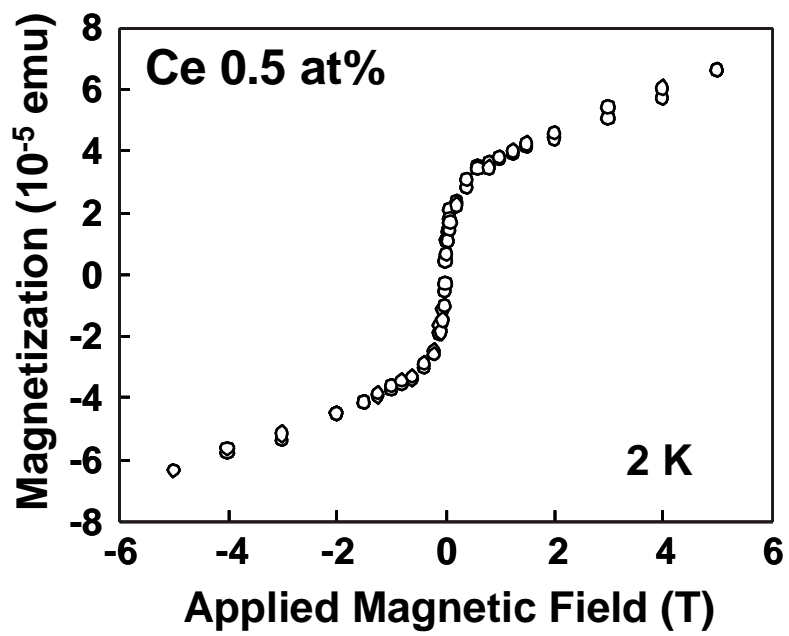
Fig. 1-4.　M-H curve of the Si:0.5 at.%Ce film grown at 740 °C measured at
2 K by SQUID

sample at the applied magnetic field below 0.05 T is larger than the paramagnetic moment of Ce^{3+} free ion calculated using Brillouin function, indicating the ferromagnetic or super-paramagnetic nature. From the temperature dependence of the magnetic susceptibility (χ-T) at the magnetic field of 0.05 T, the susceptibility increases with increasing the temperature as shown in Fig. 1-5(a). The χ-T curve has a cusp at around 180 K. And the temperature dependence of the electrical resistivity (ρ-T) curve also has a cusp at around the same temperature. This behavior is apparently different from the nonmagnetic ion, such as B- or P-doped Si. This magnetic property suggests that a spinglass-like interaction occurs in the sample. The cusp in the χ-T curve could be attributed to the frozen state of the dispersed spin. The cusp in the ρ-T curve originates from the spin fluctuations just above the spin-freezing temperature. An alternative explanation to the spin-glass is a blocking phenomenon that observed in the materials dispersed ferromagnetic particulate. To reveal the origin of the cusp, detailed magnetic and magneto-transport properties below the cusp temperature were investigated. The film was exhibited p-type conduction with a hole density of 1.6×10^{16} cm^{-3} at room temperature. A Ce^{3+} ion act as an acceptor by the substitutional incorporation. Figure 1-6 shows the magnetic field dependence of magnetization, magneto-resistance (MR), and Hall voltage measured at 100 K, which is lower than the cusp temperature. The magnetization shows abrupt increase within the magnetic field of 0.1 T, and the positive MR also increase rapidly within this magnetic filed. An anomalous Hall effect is observed and the change in slope occurs at ±0.1 T. This change also corresponds to the nonlinearity of M-H curve. This phenomenon can explain by the spin-flip scattering in spin-frozen state [24]. Below the cusp temperature, a large number of spins cooperatively freeze in random orientation. The frozen state of spins is affected by the
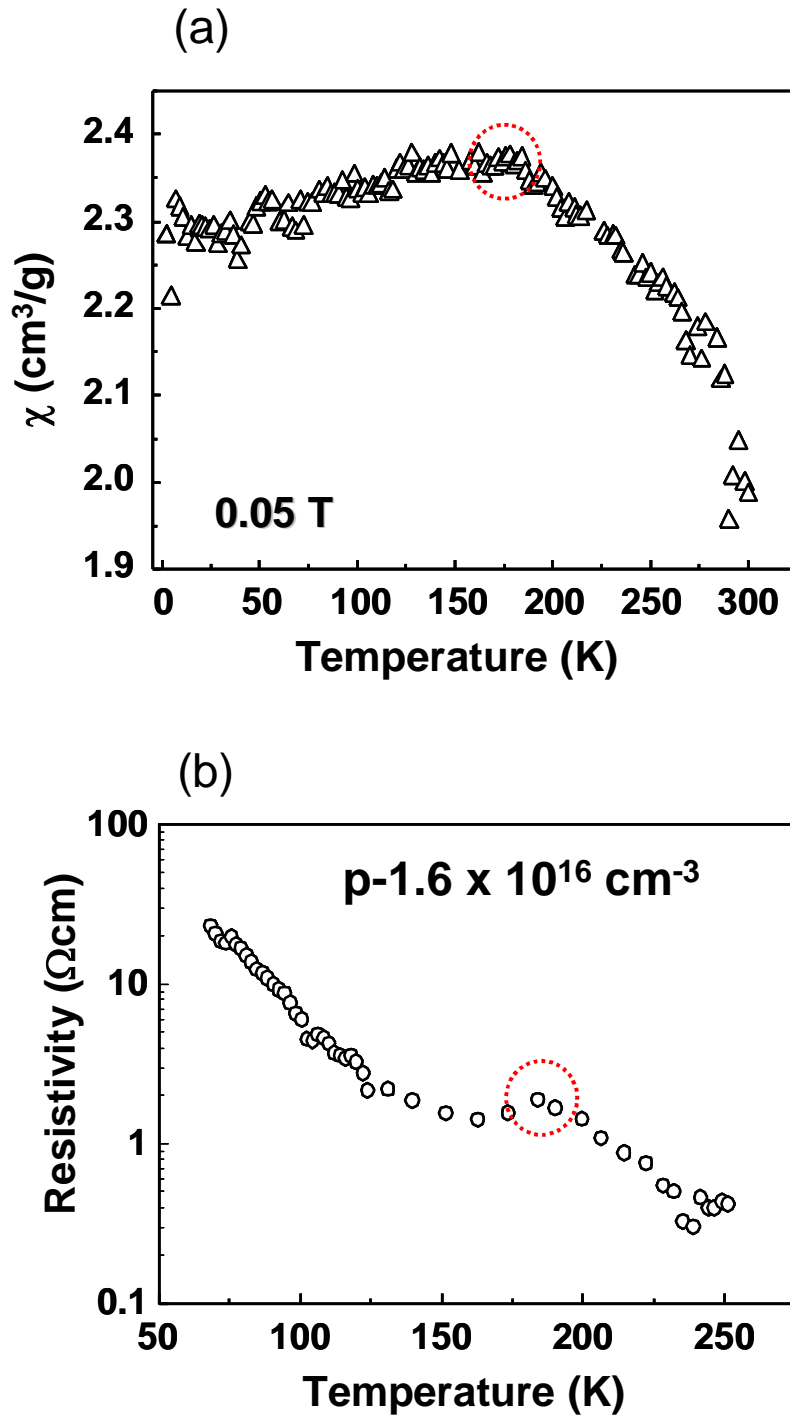
Fig. 1-5. Temperature dependence of the magnetic susceptibility (a) and the resistivity (b) of Si:0.5 at.%Ce film grown at 740 °C. Magnetic susceptibility was measured at 0.05 T.
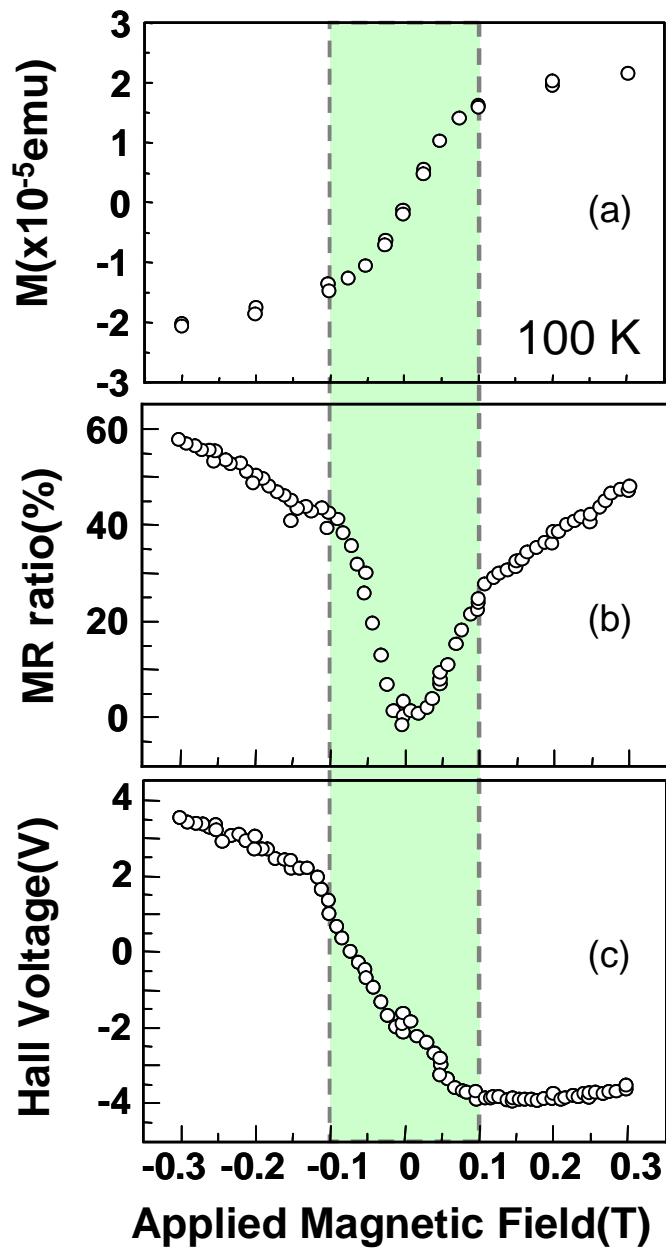
Fig. 1-6.   Magnetic field dependence of magnetization (a),
magnetoresistance (b) and Hall voltage (c) at 100 K.

external magnetic field. Therefore, the spin disorder scattering, which give rise to the large positive MR, is occurred. It is considered that these anomalous magneto-transport behaviors indicate the spin-carrier interaction.

However, the precipitation of cerium silicide ($CeSi_x$) has been observed occasionally when the growth temperature is 740 °C, as shown in Fig. 1-7. Figure 1-7(a) shows the AFM image of the film surface. Although the three-dimensional growth and large hillock were not observed in the film, unlike the sample previously mentioned, large amount of pits with the diameter of a few hundreds nanometers are recognized in the AFM image. From the cross-sectional TEM observation of the pit region, the precipitation of second phase is recognized at the bottom of the pit. Figure 1-7(b) shows the SAD pattern of the film/Si substrate interface. As shown in Figure 1-7(b), the pattern can be deconvoluted to the two patterns of the diamond (shown by solid circle) and the tetragonal (shown by dotted circle). The tetragonal structure corresponds to $CeSi_x$ ($1.75 < x < 2.00$). The tetragonal $CeSi_x$ shows ferromagnetism with the $1.75 < x < 1.85$ or nonmagnetic heavy fermion-type magnetic behavior with the $1.85 < x < 2.0$ [25–30]. Figure 1-8(a) shows the SIMS depth profile of this sample. Owing to the silicidation reaction, Ce segregates at around the film surface and the Si:Ce/Si substrate interface is not abrupt. $CeSi_x$ has various magnetic properties, such as antiferromagnetic, ferromagnetic, or heavy-fermion-type nonmagnetic states depending on the Si content x. So we can conclude that the growth temperature of 740 ºC is too high to obtain the epitaxial Si:Ce film without forming the second phase. The inhomogeneous microstructure and the compositional distribution makes it complicated to investigate the intrinsic magnetic and electrical properties of Si:Ce thin film.

(a)

Pit

20 nm

500 nm

(b)

Si 002

CeSi$_2$ 004

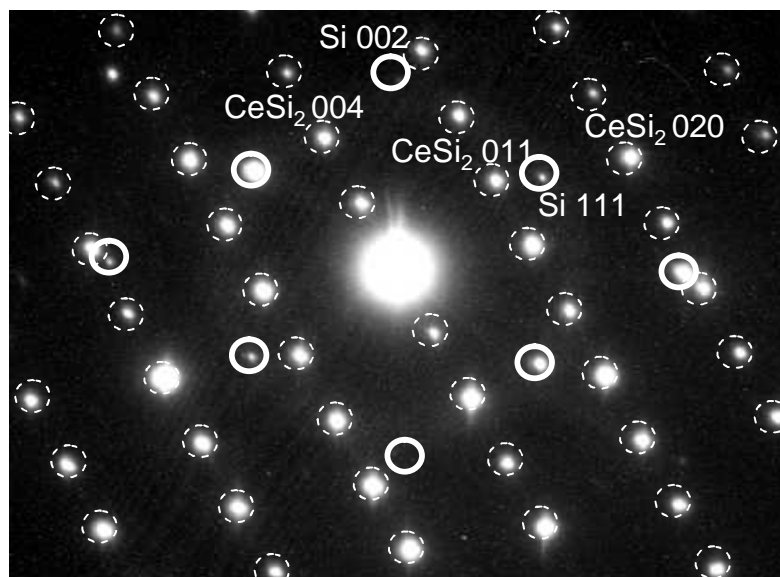CeSi$_2$ 011

CeSi$_2$ 020

Si 111
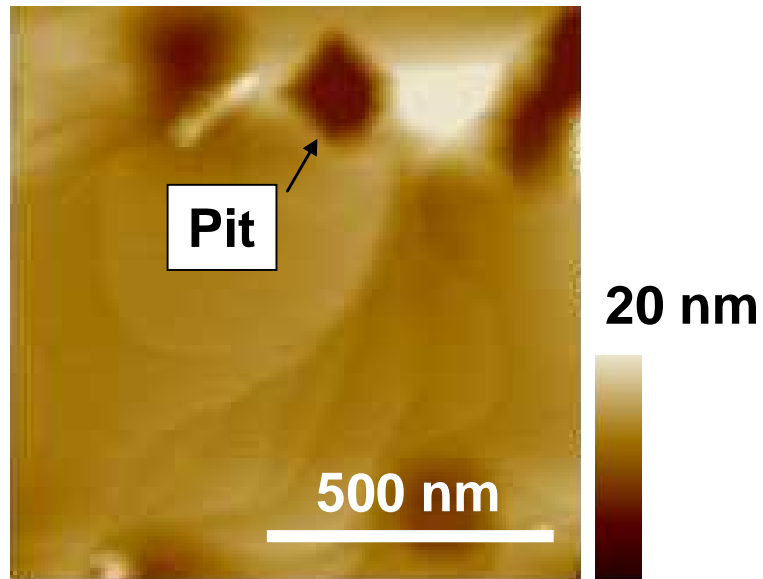
Fig. 1-7.　AFM image (a) and SAD pattern of TEM for Si:0.3 at.%Ce thin film grown at 740 °C.

Based on these situation, Terao *et al.* have worked on the low temperature MBE (LT-MBE) growth of Si:Ce thin film to suppress the precipitation of the second phase [31,32]. As a result, uniformly Ce distributed Si:Ce thin films with high crystallinity, smooth surface, and abrupt interface have been obtained as shown in Fig.1-8(b) and Fig 1-9(a). From the SAD pattern of Si:Ce region, no precipitation is observed (Fig.1-9(b)). By optimizing the growth procedure, film growth at 450 °C was successfully enabled. And also, it is revealed that the $CeSi_x$ affect the magnetic and magnetotransport properties of Si:Ce below 20 K from the investigation using epitaxial grown $CeSi_x$ film on Si(001). However, unlike the high temperature grown Si:Ce, LT-grown Si:Ce film exhibited *n*-type conduction and paramagnetic behavior in many cases. From results of XPS measurement, tetravalent Ce exists in the film much more than trivalent Ce. The tetravalent Ce atom probably occupies the interstitial site and causes the electron emission [32].

These experimental results indicate that both high concentrated region of Ce^{3+} in the film and the existence of hole may be important for the ferromagnetic Si:Ce. At present, the origin of ferromagnetic ordering remains a topic of active research. It is known that the magnetic and electronic properties of DMSs strongly depend on the distribution and local environment of the dopant.[33] Accordingly, it is important to ascertain how Ce atoms are incorporated into Si film during growth.
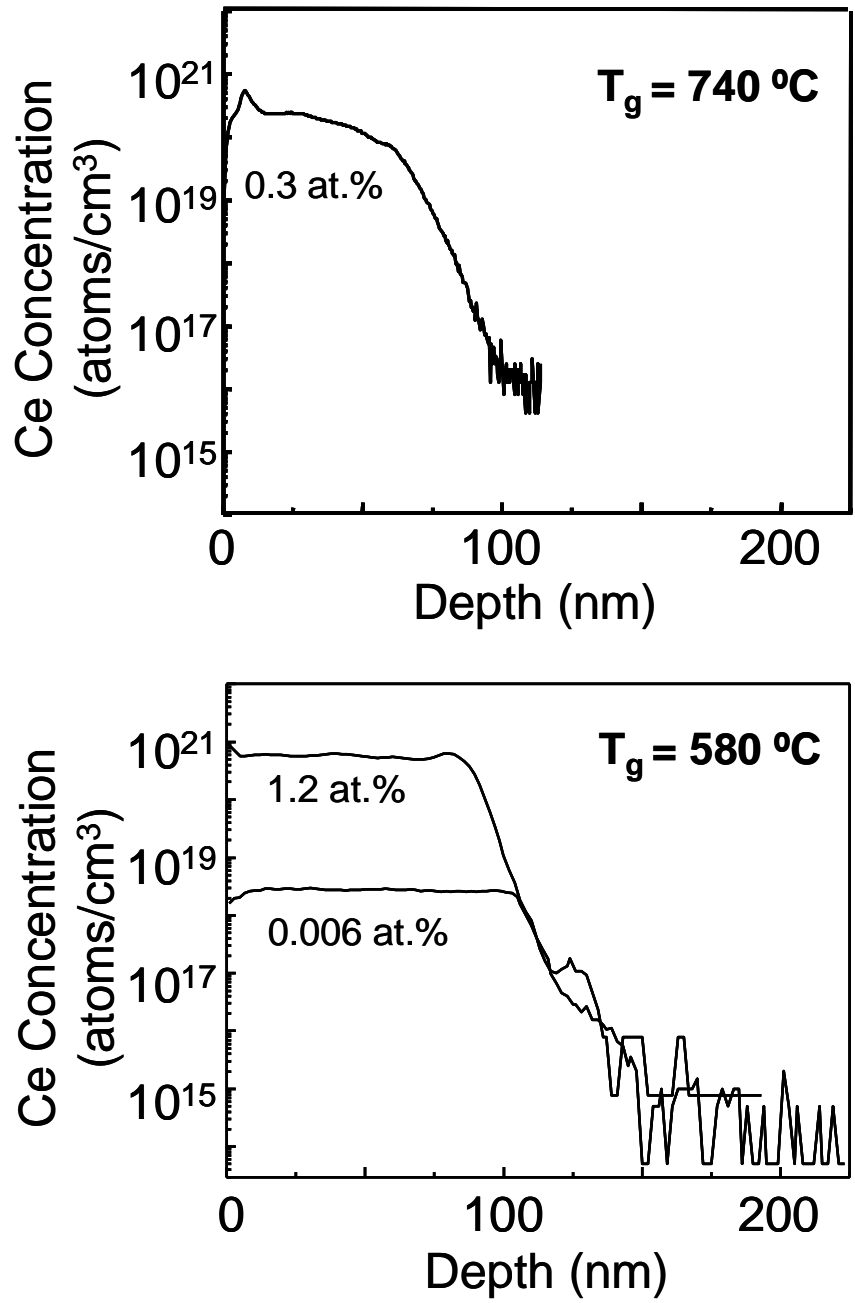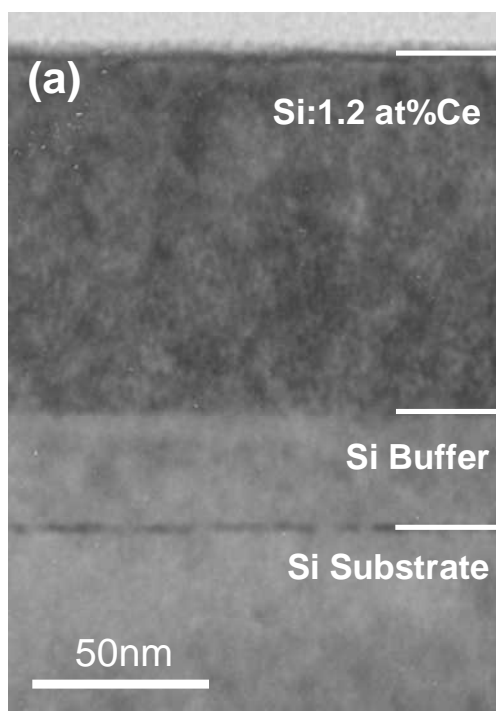
Fig. 1-8.   SIMS profiles of Ce in Si:0.3 at% Ce thin film grown at 740 °C (a) and Si:Ce films grown at 580 °C with Ce concentration of 0.006 and 1.2 at.% (b).

TEM Image

(a)

Si:1.2 at%Ce

Si Buffer

Si Substrate

50nm
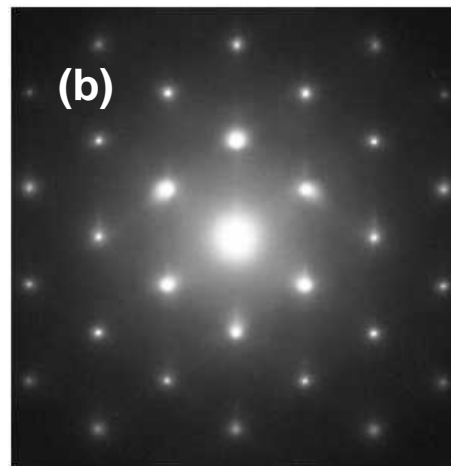
SAD Pattern

(b)

Fig. 1-9. Cross-sectional TEM image (a) and SAD pattern (b) of Si:1.2 at.%Ce film grown at 580 °C.

1.3　The aim of this work and thesis outline

The followings are listed as attractive challenges of Si:Ce.

(1) To clarify what kind of impurity levels the Ce atom forms in the Si energy band gap when the Ce atom distribute uniformly in the film at LT-growth.

(2) To investigate a effect of carrier type and carrier density for the magnetic and magnetotransport properties of Si:Ce film without changing the local crystal structure by introducing a co-dopant for shallow acceptor or donor.

(3) To make highly-Ce-doped region without precipitations.

To solve these problems, we worked on this study. In this thesis, we investigated what kind of energy levels are formed by Ce incorporation in LT-grown Si:Ce film and the control of carrier type and density using Metal-Insulator-Semiconductor (MIS) structure. Novel doping method of Ce atom was also investigated. This thesis is composed of six chapters. The outline of each chapter is shown below.

In chapter 2, Ce-related energy levels in LT-grown Si:Ce are investigated by transport measurements and dielectric measurements. In the Hall effect measurement, parallel conduction with the film and the substrate occurred. From the capacitance measurement of $Au/Y_2O_3/Si:Ce$ - MIS capacitor, n-type behavior was confirmed. In the low Ce concentration, electron density increase with increasing Ce concentration. The electrons probably arise from Si vacancies emission accompanied with Ce incorporation. Additional Ce-doping into Si causes the films to be high resistive. It is indicated that deep level traps increase with Ce increasing from the analysis of C-f and G_p/ω-f measurement. Carrier compensation by the deep level traps causes high resistivity of Si:Ce film. From the XRD measurements, decrease of lattice parameter was observed in the high resistive samples. A high concentration of vacancies would result in formation

of vacancy-vacancy and vacancy-Ce complexes. The appearance of deep level traps is attributed to the presence of these point-defect complexes.

In chapter 3, in order to investigate the effect of the hole on the magnetic interaction of LT-grown Si:Ce film, homogenous Ce distributed LT-grown Si:Ce films with *p*-type conduction have been prepared by means of codoping of Al and B. The highly hole-doped films show paramagnetic behavior. The film with metallic conduction shows distinct carrier-4*f* spin exchange interaction by analyzing the MR behavior. The *p-f* interaction energy of the metallic Si:Ce,Al and Si:Ce,B is calculated as 52 meV and 48 meV, respectively . On the basis of this result, the hole plays an important role in the magnetic properties of the Ce-doped Si thin films.

In chapter 4, in order to control the carrier type and carrier density by applying an electric field, bottom gate type Metal/ferroelectric/Si:Ce (MFS) structure was investigated. Ferroelectric materials can induce large amount of charge with a small electric field. Therefore it is suitable as a gate insulator for studying field effect. Although it was a polycrystalline film, Si:2.9at%Ce film without silicide precipitation was successfully obtained on epitaxial grown ferroelectric $YMnO_3$. We determined the induced charge density of the Si:Ce film by the ferroelectric $YMnO_3$ film from polarization measurements. The dielectric properties of bottom gate type Pt/$YMnO_3$/Si:2.9 at%Ce/Al MFS structure were investigated. The capacitor exhibits a ferroelectric type *C-V* hysteresis loop. Detailed dielectric analysis revealed that the *C-V* hysteresis was caused by both ferroelectricity and space charge. From the *P-V* measurements at 100 kHz, although ferroelectric behaviors such as remnant polarization and saturation of polarization were not recognized, the measured polarization value originated from ferroelectric $YMnO_3$ was enough to obtain the carrier inversion of Si.

In chapter 5, novel doping methods of Ce atom with high concentration are proposed. Ce-related surface reconstructions which appear during the growth are used. The novel Ce-related surface reconstruction has three-fold periodicity. As the Ce concentration is increased, the 3× surface appeared at thinner film thickness. This 3× surface structure requires a certain amount of Ce atoms to form the structure. HR-RBS analysis revealed the variation in the distribution of Ce atoms in the film in association with emergence of the 3× surface. The mechanism of the emergence of this surface reconstruction and the confinement of the structure are discussed.

Chapter 6 summarized the main results and described the mechanism of ferromagnetic behavior observed in Si:Ce films.

References

[1] J. F. Gregg, I. Petej, E. Jouguelet, and C. Dennis: J. Phys. D: Appl. Phys. **35** (2002) R121.

[2] I. Žutić, J. Fabian, and S. Das Sarma: Rev. Mod. Phys. **76** (2004) 323.

[3] H. Munekata, H. Ohno, S. von Molnar, A. Segmuller, L. L. Chang, and L. Esaki: Phys. Rev. Lett. **63** (1989) 1849.

[4] H. Ohno, H. Munekata, T. Penny, S. von Molnar, and L. L. Chang: Phys. Rev. Lett. **68** (1992) 2664.

[5] H. Ohno, A. Shen, F. Matsukura, A. Oiwa, A. Endo, S. Katsumoto, and H. Iye: Appl. Phys. Lett. **69** (1996) 363.

[6] T. Hayashi, M. Tanaka, T. Nishinaga, H. Shimada, H. Tsuchiya, and Y. Otuka: J. Cryst. Growth **175/176** (1997) 1063.

[7] T. Jungwirth *et al.*: Phys. Rev. B **72** (2005) 165204.

[8] W. Mac, A. Twardowski, and M. Demianiuk: Phys. Rev. B **54** (1996) 5528.

[9] H. Saito, V. Zayets, S. Yamagata, and K. Ando: Phys. Rev. Lett. **90** (2003) 207202.

[10] Y. D. Park, A. Wilson, A. T. Hanbicki, J. E. Mattson, T. Ambrose, G. Spanos, and B. T. Jonker: Appl. Phys. Lett. **78** (2001) 2739.

[11] Y. D. Park, A. T. Hanbicki, S. C. Erwin, C. S. Hellberg, J. M. Sullivan, J. E. Mattson, T. F. Ambrose, A. Wilson, G. Spanos, and B. T. Jonker: Science **295** (2002) 651.

[12] J. Chen, K. L. Wang, and K. Galatsis: Appl. Phys. Lett. **90** (2007) 012501.

[13] Y. Shuto, M. Tanaka, and S. Sugahara: J. Appl. Phys. **99** (2006) 08D516.

[14] F. M. Zhang, X. C. Liu, J. Gao, X. S. Wu, Y. W. Du, H. Zhu, J. Q. Xiao, and P. Chen: Appl. Phys. Lett. **85** (2004) 786.

[15] M. Bolduc, C. Awo-Affouda, A. Stollenwerk, M. B. Huang, F. G. Ramos, G. Agnello, and V. P. LaBella: Phys. Rev. B **71** (2005) 033302.

[16] T. Kasuya, T. Suzuki, and Y. Haga : J. Phys. Soc, Jap. **62** (1993) 2549.

[17] T. Kasuya, Y. S. Kwon, T. Suzuki, K. Nakahishi, F. Ishiyama, and K. Takegahara : J. Magn. Magn. Mater. **90&91** (1990) 389.

[18] N. Shibata, C. Ishii, and K. Ueda : Phys. Rev. B **52** (1995) 10232.

[19] T. Yokota, N. Fujimura, Y. Morinaga, and T. Ito: Physica E **10** (2001) 237.

[20] T. Yokota, N. Fujimura, and T. Ito: Appl. Phys. Lett. **81** (2002) 4023.

[21] T. Yokota, N. Fujimura, T. Wada, S. Hamasaki, and T. Ito: J. Appl. Phys. **91** (2002) 7905.

[22] T. Yokota, N. Fujimura, and T. Ito: J. Appl. Phys. **93** (2003) 4045.

[23] T. Yokota, N. Fujimura, T. Wada, S. Hamasaki, and T. Ito: J. Appl. Phys. **93**, (2003) 7679.

[24] A. K. Nigam and K. Majumadar : J. Appl. Phys. **50** (1979) 1712.

[25] N. Sato, H. Mori, T. Satoh, T. Miura, H. Takei: J. Phys. Soc. Jpn. **57** (1988) 1384.

[26] W. H. Lee and R. N. Shelton: Phys. Rev. B. **35** (1986) 8523.

[27] S. A. Shaheen and J. S. Schilling: Phys. Rev. B. **35** (1987) 6880.

[28] S. A. Shaheen: J. Appl. Phys. **63** (1988) 3411.

[29] S. A. Shaheen: Phys. Rev. B. **36** (1987) 5472.

[30] S. A. Shaheen and W. A. Mendoza: Phys. Rev. B. **60** (1999) 9501

[31] T. Terao, Y. Nishimura, D. Shindo, and N. Fujimura: J. Cryst. Growth **307** (2007) 30.

[32] T. Terao, K. Fujii, D. Shindo, T. Yoshimura, and N. Fujimura: Jpn. J. Appl. Phys. **48** (2009) 033003.

[33] D. Kitchen, A. Richardella, J. M. Tang, M. E. Flatte, and A. Yazdani: Nature (London) **442** (2006) 436.

2

Electrical evaluation of the energy level derived from Ce doping

2.1   Introduction

The introduction of impurity atoms within the semiconductor has been the principal method for controlling the properties, such as optical, electrical, and magnetic properties. In DMSs, it is important to evaluate the energy levels formed by magnetic impurities in the host semiconductors band gap. Because the acceptor (donor) state introduced by magnetic impurity interact with valence (conduction) band and strongly affect the optical, electrical, and magnetic properties. For the detection of impurity energy levels, transport properties and optical properties are often investigated. Dielectric properties, especially capacitance measurement are also used for the evaluation of energy levels. As a typical method, deep level transient spectroscopy (DLTS) is used for compound semiconductor based DMSs [1-3]. Rare-earth doped Si , especially Er-doped Si is also well studied about the Er-related levels by DLTS for the optical device application. Er-doped Si has been considered as a promising Si-based light-emitting material since the first report of photoluminescence from Si:Er in 1983 [4]. The rare-earth Er ion is well known to emit photons at the wavelength around 1.53 μm, which corresponds to the absorption minima of the optical fibers. Rare-earth doped semiconductors are expected to produce highly efficient electroluminescent devices due to the specific optical properties of rare-earth materials such as a sharp, intense and

22

temperature-independent emission due to the intra-4f shell transitions. Extensive experimental and theoretical studies have been performed not only on the Si:Er system but also other combination of host semiconductor and rare earth elements are studied. However, Ce-related levels in Si have not studied yet. And also, the relationship between the Ce-related levels and the magnetic properties has not studied.

Although LT-MBE-grown Si:Ce thin films have a uniform Ce distribution, very smooth surface and abrupt interface, the mobility of the Si:Ce is often low. As a result, the transport properties show parallel conduction with substrate. It is often difficult to evaluate only the film transport properties. Dielectric measurement such as capacitance measurement is useful in this situation. The aim of this work is to investigate how the carrier type and the carrier density change for the systematic increase of Ce concentration and what kind of energy levels the Ce introduce.

2.2   Experimental

Si:Ce epitaxial films were deposited on Si (001) substrate by solid source MBE. The Si substrate was chemically cleaned with SemicoClean 23 (Furuuchi Chemical). After immersion in 1% HF solution for 3 min, the substrate was inserted into an ultrahigh-vacuum MBE chamber. The sample was carefully outgassed at 600 °C and β-SiC was intentionally formed at 850 °C to fix carbon at the interface between the Si buffer layer and the substrate. After growing the 30-nm-thick Si buffer layer at 580 °C, the substrate was then annealed at 750 °C in order to form a step and terrace surface structure. A 100-nm-thick Si:Ce layer was grown on the Si buffer layer at 580 °C. For the deposition of the Si:Ce layer, Si and Ce were simultaneously evaporated by using

high-temperature Knudsen cells. A 3-nm-thick Si capping layer was eventually grown at the same temperature as that of the Si:Ce layer. During the deposition the pressure was below 7×10^{-10} torr. The deposition rate of Si was fixed at 100 nm/h. Ce concentration of the films was varied from 0.003 to 0.9 at.% by adjusting the deposition rate of Ce. The substrate temperature was measured with a thermocouple and pyrometer.

After the Si:Ce deposition, the sample was exposed in air. After 1 min. dipping in 1% HF solution to remove the native oxide layer, the sample was transferred to another PLD chamber quickly. 18-nm-thick Y_2O_3 were deposited on Si:Ce using pulsed laser deposition (PLD) system for the gate insulator. A Y_2O_3 taiget was placed at a distance of 4 cm from the substrate and ablated by ArF excimer laser pulsed with a fluency of 100 mJ/cm^2 in a repetition rate of 1 Hz. The substrates were heated by a semiconductor laser (cw, λ=808 nm). An Y_2O_3 sintered ceramic target was used. A two-step growth process was used to prevent the surface oxidation of Si:Ce. At the initial stage of the film growth, 4 ML-thick film was deposited at 450 °C in a high vacuum (1.0×10^{-8} Torr) to fabricate the layer to protect against surface oxidation of the Si:Ce, and subsequent Y_2O_3 film was deposited in oxygen atmosphere (1.0×10^{-6} Torr) at 500 °C. Au gate electrode with the area of 3×10^{-4} cm^2 were deposited by electron beam (EB) evaporation through a shadow mask and Au backside electrode were formed by the DC-sputtering for making MIS capacitors. After the metal deposition, no annealing process was performed.

All electrical measurements were performed in the dark in a shielded probe station using a HP 4140B picoammeter for the current-voltage characteristics and a HP4284A LCR meter for the admittance measurements. All voltages are given with respect to the gate electrode. Capacitance-Voltage (*C-V*) and Conductance-Voltage

(*G-V*) characteristics were measured with an LCR meter (HP4284A) by applying a small alternating voltage signal of 100 mV amplitude and at various frequencies (20 Hz – 1 MHz).

Surface morphology and structure were evaluated by *in situ* RHEED. The crystal structure of the film was evaluated by in situ reflection high energy electron diffraction and X-ray 2θ-ω diffraction (XRD). The composition of the films was evaluated by electron probe microanalysis (EPMA) and SIMS measurement..

2.3   Results and Discussion

### 2.3.1   Crystallinity of LT-grown Si:Ce thin films

As mentioned in chapter 1, LT-growth of Si:Ce enable to distribute the Ce atom uniformly in the film and to make flat surface, abrupt interface. As shown in Fig. 1-8 (b), uniformly distributed Ce was confirmed by the SIMS measurement of Si:1.2at.%Ce film grown at 580 °C. And also, no precipitation such as silicide was observed by the TEM observation of this sample (Fig. 1-9).

Figure 2-1 shows the *in situ* RHEED pattern of 100 nm-thick Si:Ce surface grown at 580 °C with the Ce concentrations of 0 (a), 0.003 (b), 0.015 (c), 0.09 (d) and 0.9 at.% (e) respectively. Below 0.09 at.% the surface shows 2×1 streak pattern throughout the film growth. On the other hand, 0.9 at.% Ce-doped sample shows defused 3× pattern. It is known that this triperiodic surface caused by Ce atom diffusion to the surface to relax the lattice strain. This 3× surface changes to 2×1 surface by deposition of Si cap layer. We describe this 3× surface in chapter 5 in detail. In these RHEED pattern, no

precipitation of secondary phase such as Cerium silicide was observed.

Figure 2-2 shows the 2θ-ω narrow scanned XRD profiles near 004 diffraction peak for the LT-grown Si:Ce films. All the peaks are asymmetric and the interference fringes are observed indicating that the films have very smooth surface and abrupt interface. Below 0.015 at.%, 004 diffraction from the Si:Ce film is at a lower angle than that of Si substrate, suggesting that the lattice constant of the Si:Ce film normal to the film surface is expanded due to the substitution of Ce ion with a larger atomic radius than that of Si. On the other hand, above 0.09 at.%, 004 diffraction from the Si:Ce film is at a higher angle than that of Si substrate. Because the atomic radius of a Ce atom is larger than that of Si atom (187 pm and 117 pm, respectively) the impurity causes positive strain in both the substitution and interstitial state. Therefore, we can assume that there are some nanometer-size-precipitates, pores or/and vacancies formed in the epilayer, resulting in a negative volume change.

(a) Ce 0 at%
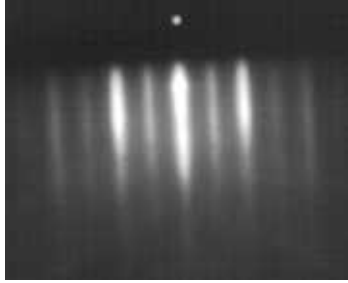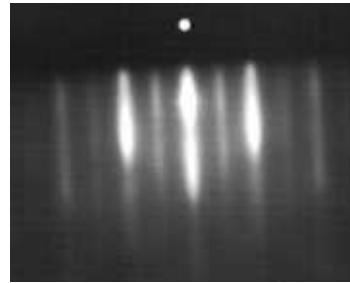
(b) Ce 0.003 at%
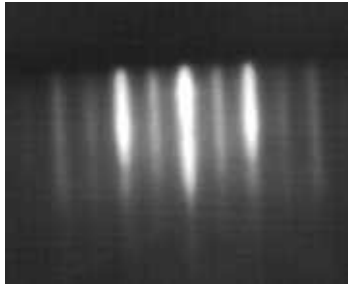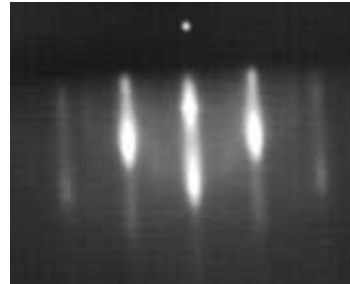
(c) Ce 0.015 at%

(d) Ce 0.09 at%
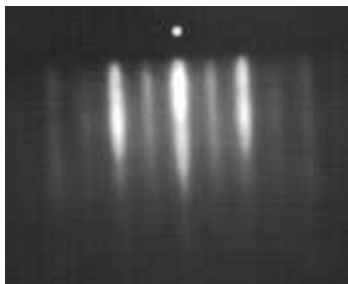

(e) Ce 0.9 at%

Fig. 2-1.   *in situ* RHEED pattern of 100 nm grown Si:Ce thin films grown at 580 °C for Ce concentrations of 0 at.% (un-doped)(a), 0.003 at.% (b), 0.015 at.% (c), 0.09 at.% (d), and 0.9 at.% (e), respectively. Incident direction of the electron beam was parallel to [110] direction.
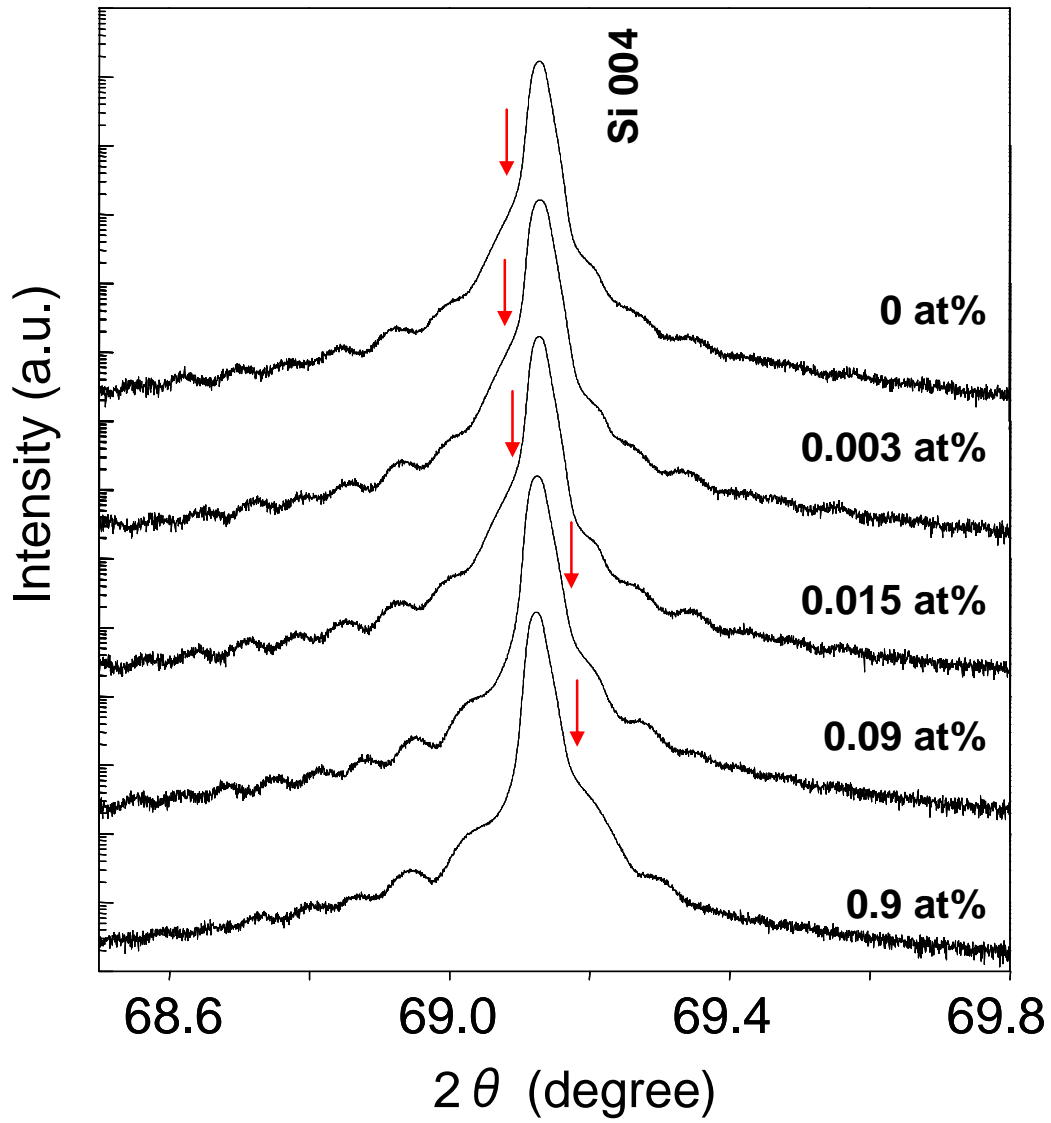
Fig. 2-2. 2θ-ω XRD profiles near Si 004 diffraction of Si:Ce films grown at 580 °C.

2.3.2 Transport properties and magnetic properties

Figure 2-3 shows the results of Hall effect measurements made for the 100 nm-thick Si:Ce thin films grown on high resistive un-doped Si(001) substrates. The temperature dependence of the sheet resistivity, the mobility and the sheet carrier density has the same dependency of the Si substrate at high temperature region. This could be because of the parallel conduction both the film and the substrate [5] or two-dimensional conduction at the film/substrate interface. At low temperature, all the film show high resistivity. The switching temperature is respectively, 180 K for the Ce un-doped film, 160 K for the 0.003 at.% and 0.015 at.%, 230 K for the Ce 0.09 at.%, and 190 K for the 0.9 at.%. All the film show n type conduction. Below switching temperature, because of low mobility and low sheet carrier concentration accurate measurement is difficult. Therefore it is difficult to evaluate the conduction properties of LT-grown Si:Ce films.

Figure 2-4 shows the result of magnetization measurement at 2 K by SQUID. Magnetization does not show monotonically increase for Ce atom increase. Si:0.09at.%Ce film shows antiferromagnetic or diamagnetic behavior. Although Si:0.9at.%Ce film soon after depositing has exhibited ferromagnetic M-H curve, the ferromagnetic behavior disappeared after a period of time. After the disappearance of ferromagnetism, paramagnetic response is observed in the Si:0.9at.%Ce film.
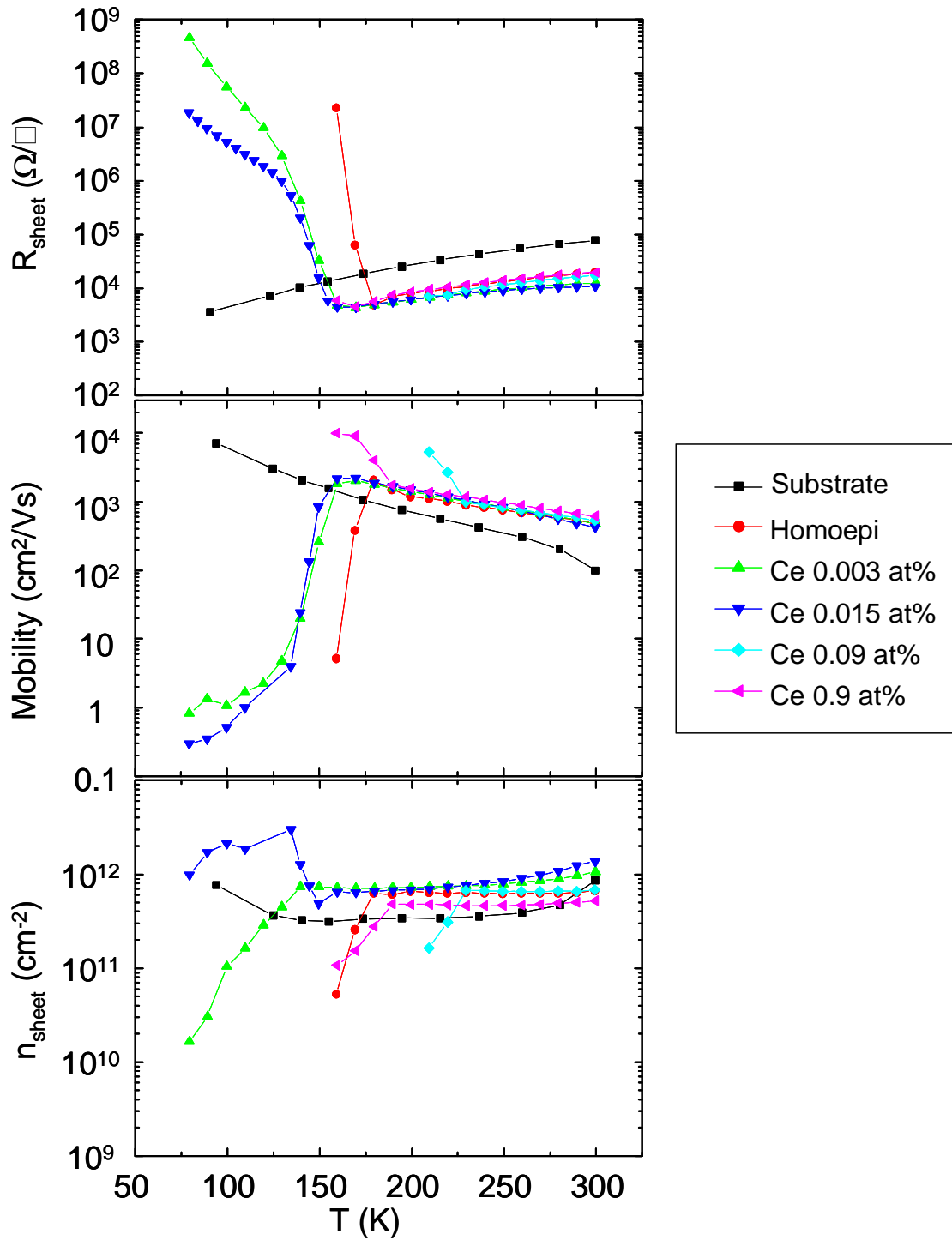
Fig. 2-3. Temperature dependence of sheet resistivity (a), mobility (b), and sheet carrier density (c) of Si:Ce thin films grown at 580 °C on the high resistivity Si(001) substrate.
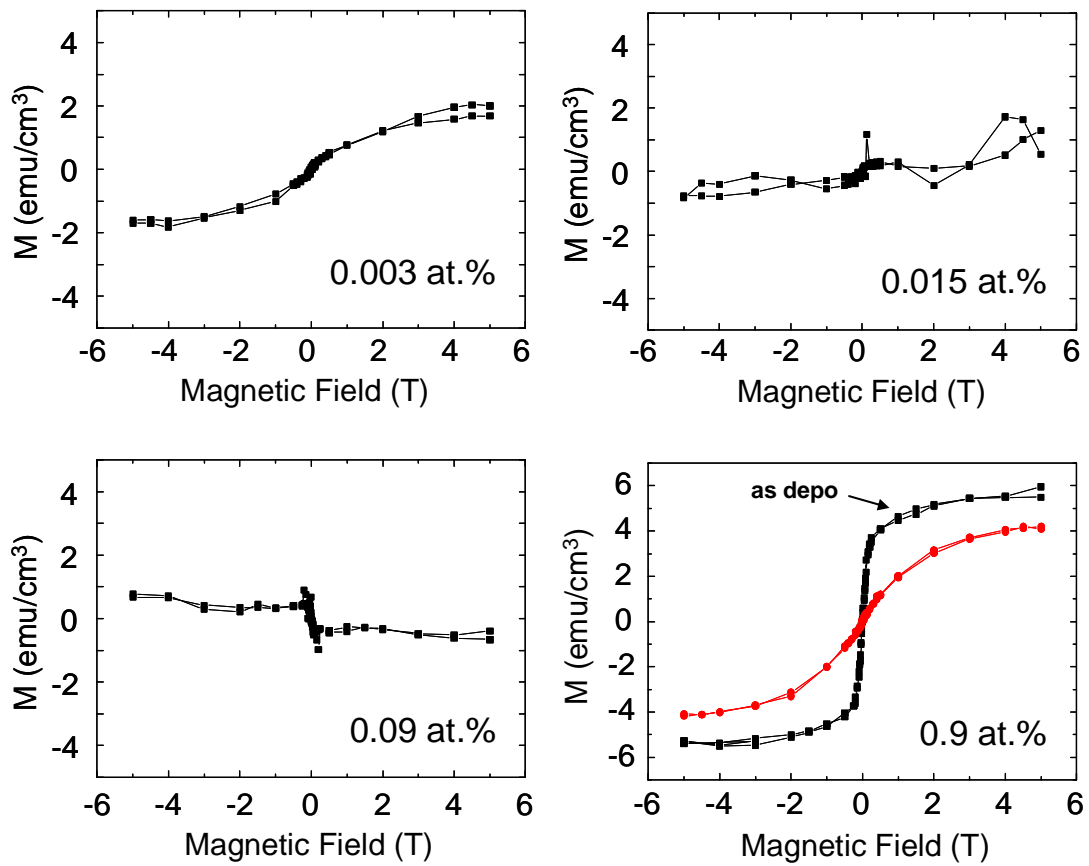
Fig. 2-4.   M-H curves of Si:Ce thin films grown at 580 °C on the high resistivity Si(001) substrate. Mearuement temperature is 2 K. External magnetic field is applied parallel to the film surface.

2.3.3 Fabrication of MIS capacitors

By the deposition of gate insulator and electrode, MIS capacitors were fabricated for these LT-grown Si:Ce films. After the 18 nm-thick Y_2O_3 film deposition by PLD, a streak pattern for the Y_2O_3 film was observed in the *in situ* RHEED observation. The streak pattern does not change in any directions of electron beam incidence. This means that the Y_2O_3 film is not an epitaxial one, which is [111]-oriented polycrystalline film. Figure 2-5 and shows the 2θ-ω wide scanned XRD profiles from the MIS capacitors. The 222 diffraction of Y_2O_3 is confirmed. No precipitation of other phase was observed.

Fig. 2-5.　2θ-ω XRD profiles of Si:Ce MIS capacitors with the Ce concentraton of 0 at.% (a), 0.003 at.% (b), 0.015 at.% (c), 0.09 at.% (d) and 0.9 at.% (e).

2.3.4 Capacitance-voltage characteristics of Si:Ce MIS capacitors

The capacitance-voltage measurements performed on the Au/Y_2O_3/Si:Ce MIS capacitor for various ac frequencies in the range of 1 MHz – 20 Hz at room temperature. In Fig.2-6, the high frequency *C-V* characteristics at 100 kHz 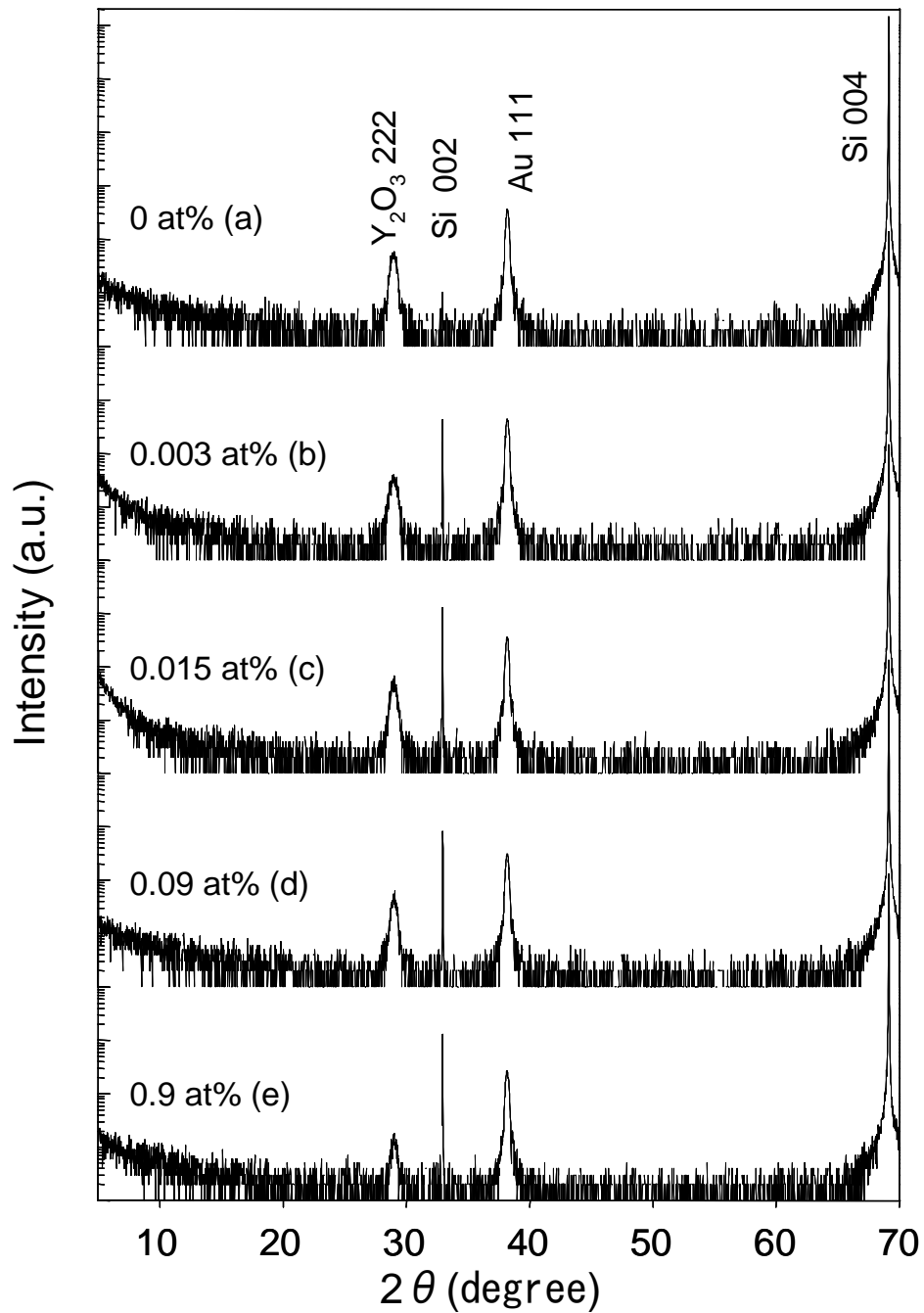of Ce concentration range from 0 to 0.015 at.% are shown. The curves show a counterclockwise hysteresis. It is likely to be due to the origins described below. (1) Mobile ions such as Na^+ and K^+ mobile in the insulator by application of dc bias, and then the mobility of ions cause a time delay with the dc bias scan. (2) Another layer such as SiO_2 or silicate are likely formed at the Y_2O_3/Si:Ce interface by the unintentional oxidation of Si:Ce surface. Two layer stack of Y_2O_3 and interface layer causes charge accumulation at the interface by Maxwell-Wagner effect. This interfacial polarization causes counterclockwise hysteresis. (3) Charge injection from the gate electrode to charge traps of Y_2O_3. In these three origins, case (1) is less likely to be the cause. Because we measure the *C-V* at room temperature and previous report of Y_2O_3/Si do not show the drift type hysteresis. It is considered that case (2) or case (3) is likely to be the cause of hysteresis.

In the Ce un-doped Si capacitor, permittivity of Y_2O_3 calculated at accumulation state is 7.4. This value is rather small compared to the values of 13-18 reported in the literature [6]. Literature reports argue that yittrium deficiency and/or porous films could result in low permittivity values of 4-5 [7,8]. Our experimental results show that the samples under study exhibit no porosity. However, the films are probably oxygen deficient, since the initial layer is grown in UHV at very low O_2 partial pressure (~10^{-8} Torr), which could explain the low permittivity values. In addition, the presence of an interfacial SiO_x layer is reported at Y_2O_3/Si interface [9,10]. It is considered to be cause

of low permittivity that existence of low dielectric constant layer at the Y_2O_3/Si:Ce interface or poorness of the crystal quality of Y_2O_3 film.

Maximum depletion layer width (W_{max}) and minimum capacitance in inversion state (C_{min}) are calculated from the following equations using a net donor concentration N_D' =N_D-N_A,

$$W_{\max} = \sqrt{\frac{4\varepsilon_s k_B T \ln(N_D^{'}/n_i)}{q^2 N_D^{'}}} , \qquad (2\text{-}1)$$

$$C_{\min} = \frac{\varepsilon_i}{d + (\varepsilon_i / \varepsilon_s)W_{\max}} , \qquad (2\text{-}2)$$

By fitting the measured inversion capacitance to minimum capacitance at inversion state of ideal *C-V* curve (Eq.(2-2)), we deduced the W_{max} and N'_D using Eq.(2-1). Inset of Fig.2-6 is the fitted result of *C-V* characteristics of Ce un-doped MIS capacitor. Table 1 is the result of calculated parameters of Si:Ce MIS capacitors. Calculated net electron density of Ce un-doped sample is 2.8×10^{17} cm^{-3}. The origin of this electron is likely to be due to the existence of point defect in Si film. The electron concentration increases with increasing Ce concentration. When the Ce atom is incorporated to Si crystal, point defects would generate. It is expected that when a Ce atom substitute the Si site Ce atom act as acceptor because of the trivalent state. However Si:Ce film show *n*-type characteristics. It is considered that the number of electron generated from point defects is greater than the hole emitted from substituted Ce. If the Si:Ce layer is *p*-type conduction, the MIS capacitor will become buried-channel MIS structure, and high frequency capacitance of the inversion side will be 0.08 µF/cm^2 at a maximum because all the 100 nm-thick Si:Ce layer act as channel. Furthermore, positive shift of *C-V* curve will be confirmed. However measured capacitance of inversion side is larger than 0.08 µF/cm^2 and apparent positive shift of *C-V* curves are not observed. Therefore Si:0.003

at.% Ce film and Si:0.015 at.%Ce film are considered to be *n*-type.

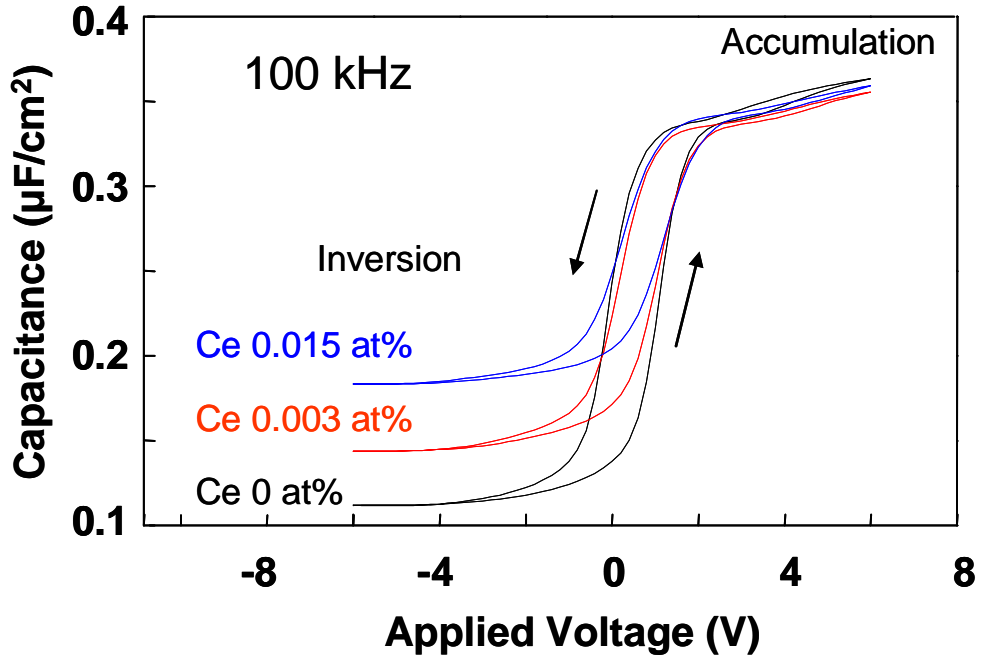Fig. 2-6.　Capacitance-voltage characteristics of Si:Ce MIS capacitors at 100 kHz.

Table 2-1.　Calculated carrier concentration *n* and maximum depletion width W_{max} of Si:Ce MIS capacitors.

Ce concentration (at.%)	Carrier concentration *n* (at.%)	Maximum depletion width W_{max} (nm)
0	2.8×10^{17}	63
0.003	6.5×10^{17}	43
0.015	1.5×10^{18}	27

Figure 2-7 shows a frequency dependence of *C-V* characteristics of Ce concentration range from 0 to 0.015 at.%. In all the samples, the accumulation capacitance do not show frequency dispersion and almost constant. On the other hand, the capacitance of inversion side increases with decreasing measurement frequency. Minority carrier is able to respond to the ac signal at low frequencies. Therefore formation of inversion layer is indicated.

For 0.015 at.% Ce doped sample, capacitance increase from depletion region to inversion region is small and almost flat. Figure 2-8 shows gate voltage dependence of equivalent parallel conductance measured at 2 kHz. The equivalent parallel conductance of depletion and week inversion exhibits constant value with applied voltage although in 0 at.% and 0.003 at.% samples equivalent parallel conductance goes through a peak in weak inversion and drops to a very low value in strong inversion. When generation and recombination through bulk trap levels dominate the loss, equivalent parallel conductance does not go through a peak as a function of gate bias in weak inversion because the loss due to this process is independent of gate bias. This bias independence results from the bias independence of hole and electron densities at the crossover point, where the Fermi level crosses bulk trap levels located near midgap [11]. In strong inversion, the equivalent circuit of these MIS capacitor is shown in Fig.2-9 at frequencies intermediate between high and low. In this equivalent circuit, C_{ox} is the gate oxide capacitance; G_{ox} is the gate oxide parallel conductance; C_D is the depletion capacitance; and G_{gr} is the conductance of generation and recombination through bulk traps with energy level located near midgap. Using this equivalent circuit, in strong inversion, the admittance of the MIS capacitor is described as the follows.

$$Y_m = \frac{G_{ox}G_{gr}(G_{ox}+G_{gr})+\omega^2(G_{gr}C_{ox}{}^2+G_{ox}C_D{}^2)}{(G_{ox}+G_{gr})^2+\omega(C_{ox}+C_D)^2} + j\omega\frac{G_{ox}{}^2C_D+G_{gr}{}^2C_{ox}+\omega^2C_{ox}C_D(C_{ox}+C_D)}{(G_{ox}+G_{gr})^2+\omega(C_{ox}+C_D)^2}$$

$$(2\text{-}3)$$

In the frequency range from low to intermediate, generation-recombination conductance G_{gr} is treated as constant. Fitting this equation to the *C-f* and G_p/ω-*f* curves in the strong inversion (applied -6 V), G_{gr} was obtained. Fitting results are shown in Fig.2-10. Obtained G_{gr} for the each Ce concentration is shown in Fig.2-11. In the intermediate frequency region, capacitance and equivalent parallel conductance are well fitted in all samples. Generation-recombination conductance increases with Ce concentration increasing. Generation-recombination current increases with increasing midgap trap level density. Therefore, it is considered that midgap trap level density increases with incorporated Ce concentration increasing. It is reported that rare earth elements (Er, Tb and Yb) in Si form deep energy levels [12-15]. Therefore, it is highly possible that Ce contributes to the formation of midgap trap levels.
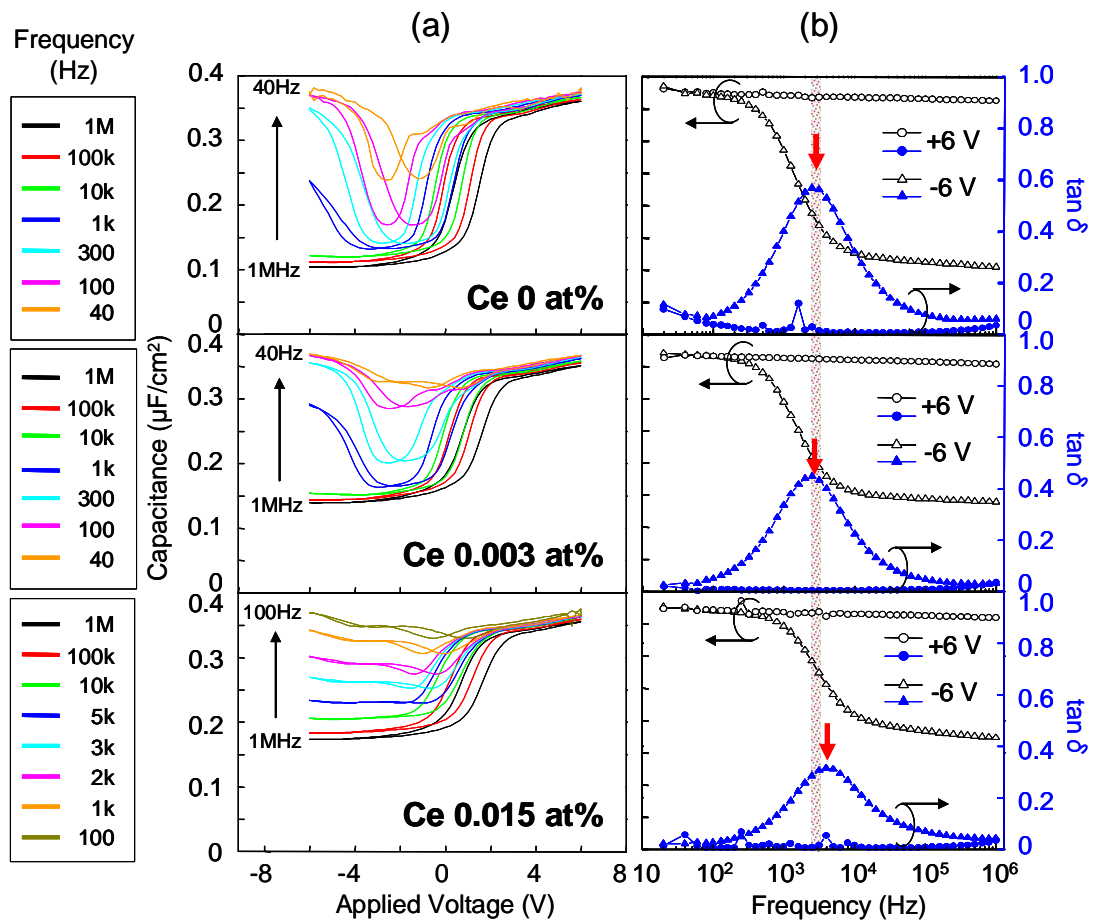
Fig. 2-7.   Frequency dependence of Si:Ce MIS capacitors with low Ce concentration.
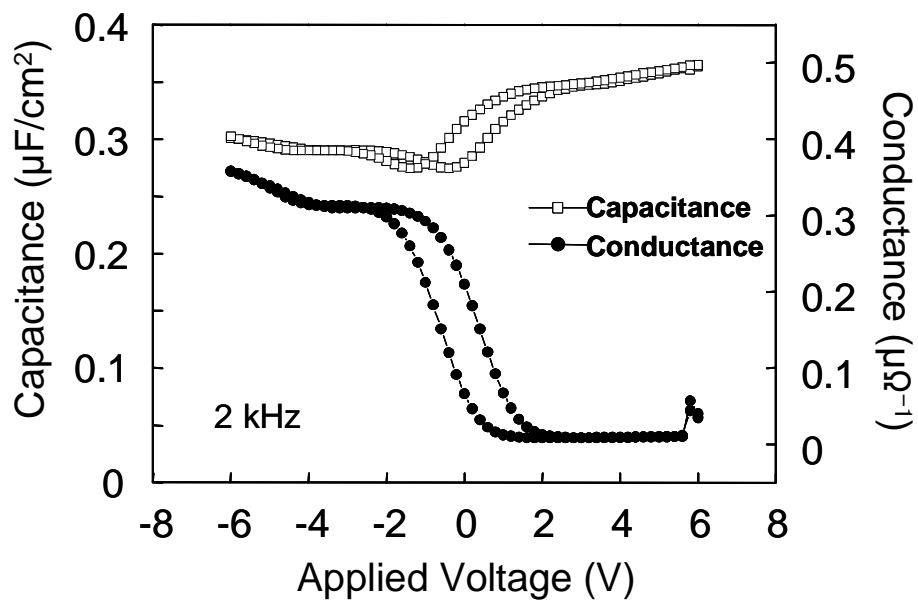
Fig. 2-8.   Capacitance-voltage and conductance-voltage characteristics of
Si:0.015 at.%Ce MIS capacitor at 2 kHz.

Au

Insulator Y$_2$O$_3$ $\quad$ C_{ox}

Si:Ce

C_D

Equivalent Circuit

G_{ox}

Strong Inversion

$\mathbf{G_{gr}}$

Generation-Recombination
Conductane

Fig. 2-9. Equivalent circuit of Si:Ce MIS capacitors at the strong inversion state.
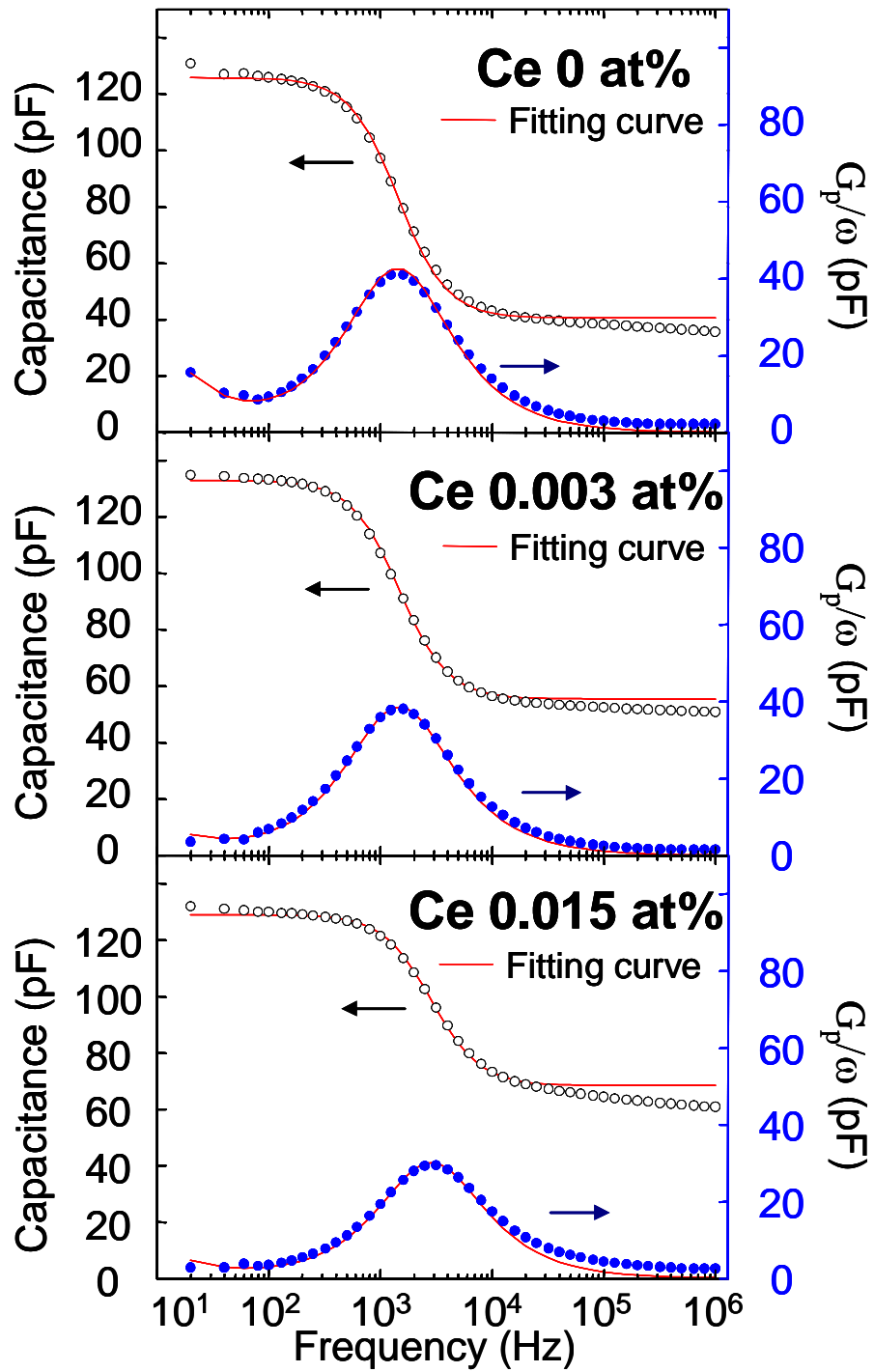
Fig. 2-10.   Fitting results of *C-f* and *Gₚ/ω-f* characteristics of Si:Ce MIS capacitors with low Ce concentration.
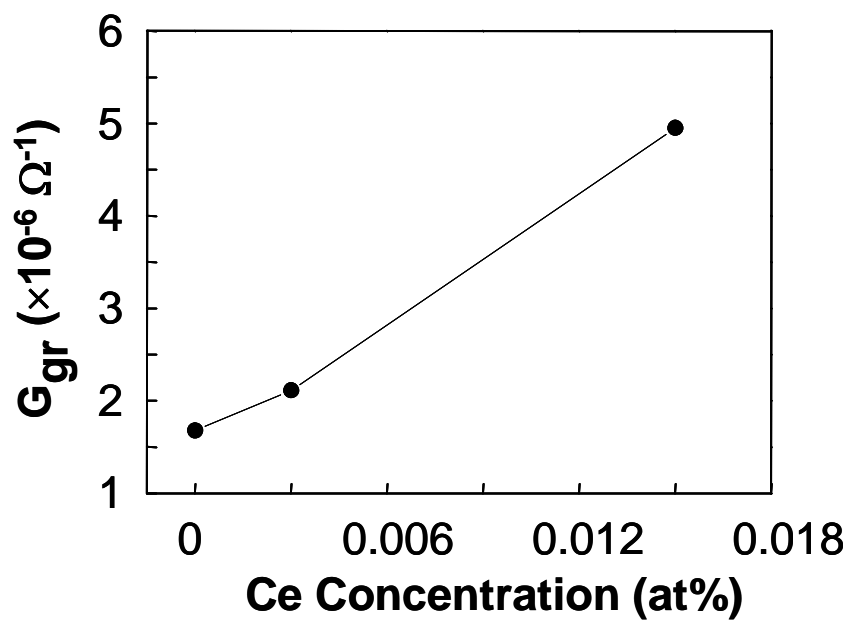
Fig.2-11. Calculated generation-recombination conductance of Si:Ce versus doped Ce concentration.

Next, *C-V* characteristics of 0.09 and 0.9 at.% Ce-doped samples are shown in Fig.2-12 and Fig.2-13. Unlike the 0.003 and 0.015 at.% Ce doped samples, not only inversion capacitance but also accumulation capacitance show frequency dispersion. As the cause of this phenomenon, the following two possibilities are considered.

(1) Deep level traps increase with increasing Ce concentration. As a result, Si:Ce film become high resistive because of strong compensation effect and carrier do not follow to ac signal at high frequency.
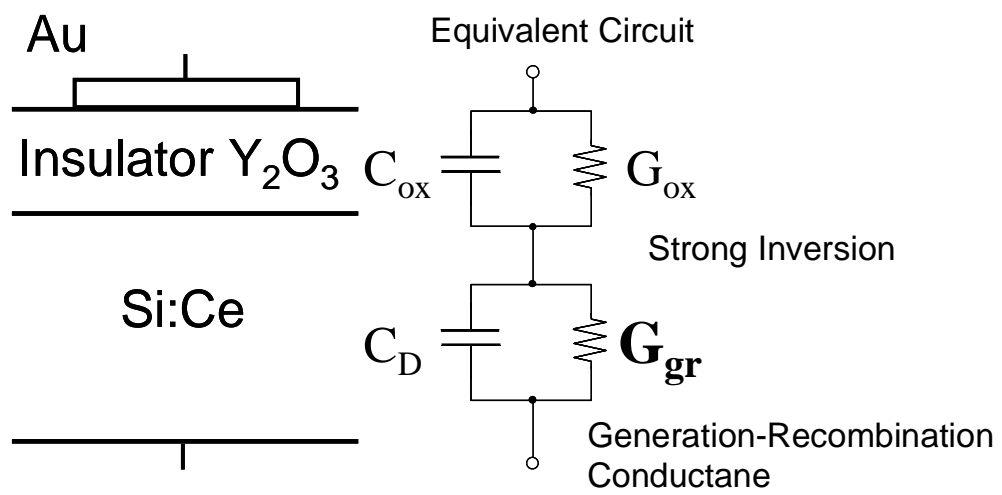
(2) Ce is incorporated as acceptor and Si:Ce layer become p-type. The MIS capacitors become deeply-buried channel structure.

In the high frequency *C-V* of deeply-buried channel structure, the channel carrier need generation-recombination process because majority carrier in the channel is not supplied from back ohmic electrode. Therefore both inversion and accumulation capacitance disperse. In the case (1), high frequency capacitance exhibit series capacitance of gate insulator and 100 nm-thick Si:Ce layer, that is 1.0×10^{-7} pF/cm^2. Meanwhile, in the case (2), high frequency capacitance exhibit series capacitance of gate insulator, Si:Ce layer, and pn junction of Si:Ce-Si buffer layer. The value is expected to be lower than 1.0×10^{-7} pF/cm^2. For the 0.09 and 0.9 at.% Ce doped samples, the series capacitance and the film thickness of semiconductor side are calculated from the capacitance at 1 MHz and low frequency capacitance. Calculated value is 0.7×10^{-7} pF/cm^2 and 110 nm. There is a possibility that both cases occur,

From the XRD measurements, above 0.09 at.% Ce doped samples exhibit lattice shrinking with the Ce doping. Given the experimental result, there is possibility that complex defects such as vacancy-vacancy or vacancy-Ce form in the Si:Ce film. Generally these complex defects in Si often form deep energy level. Therefore case (1)

is more likely to be cause of frequency dispersion.

Ce 0.09 at%

Fig. 2-12. Frequency dependence of Capacitance-voltage characteristics of Si:0.09 at.%Ce MIS capacitor. Left graph is *C-V* curves at various frequencies and right graph is *C-f* and *tanδ- f* curves at +6 V (circle), 0 V (square), and -6 V (triangle).
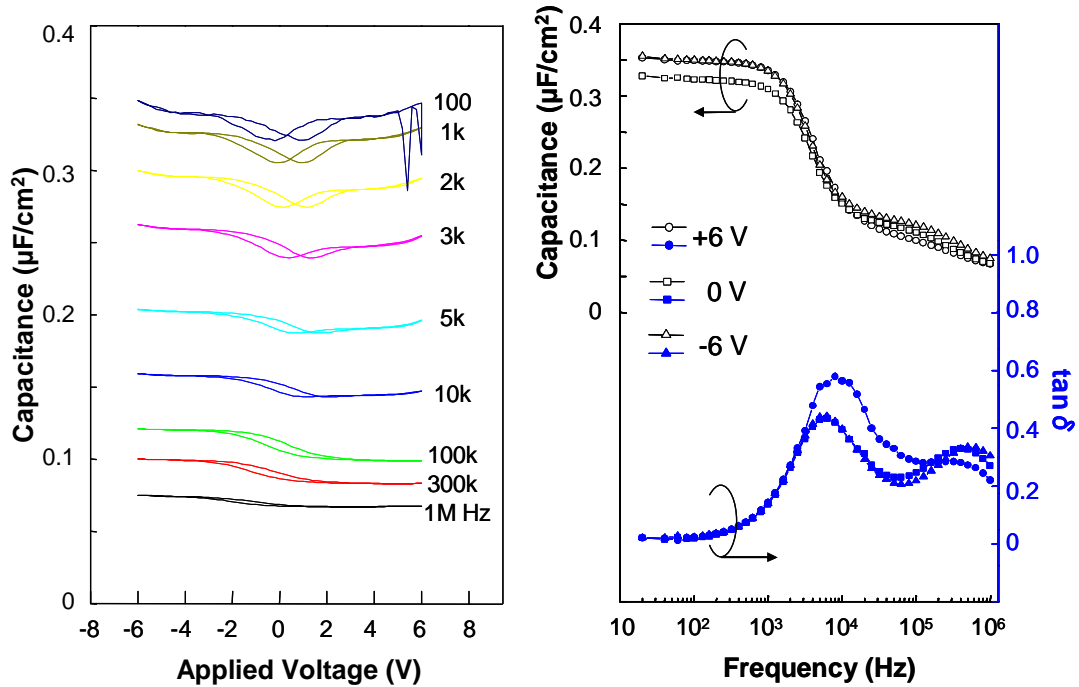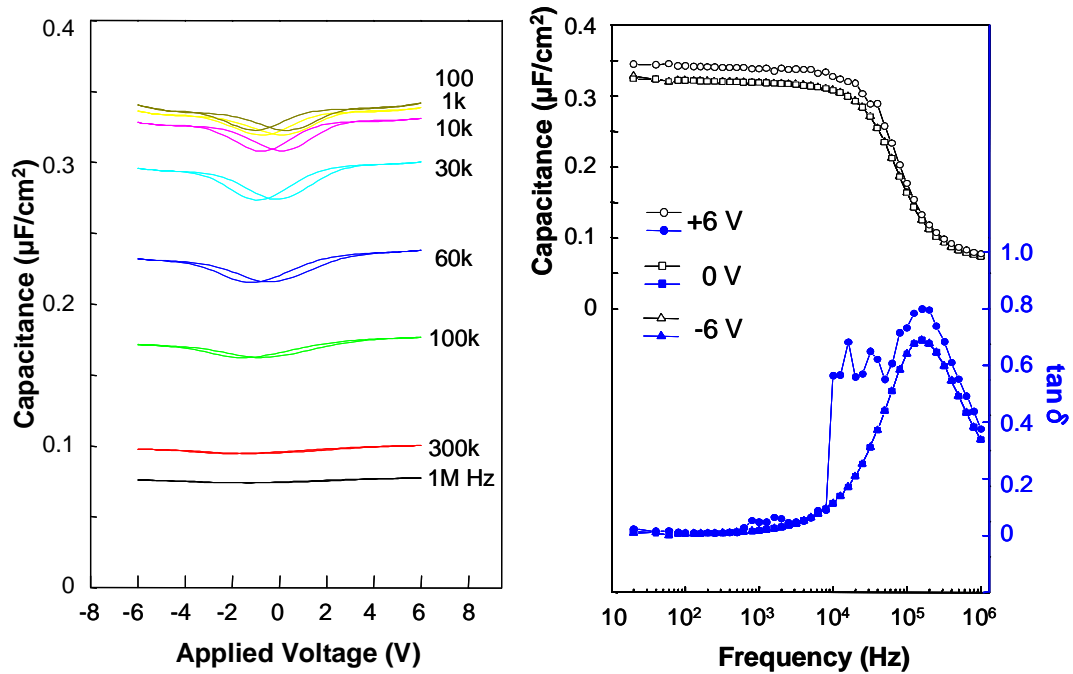
Fig. 2-13. Frequency dependence of Capacitance-voltage characteristics of Si:0.9 at.%Ce MIS capacitor. Left graph is *C-V* curves at various frequencies and right graph is *C-f* and *tanδ- f* curves at +6 V (circle), 0 V (square), and -6 V (triangle).

2.4 Conclusion

We investigate the change of carrier type and carrier density associated with Ce incorporation of LT-grown Si:Ce MIS capacitor using capacitance-voltage measurements. In the low Ce concentration, electron density increase with increasing Ce concentration. The electrons probably arise from Si vacancies emission accompanied with Ce incorporation. Additional Ce-doping into Si causes the films to be high resistive. It is indicated that deep level traps increase with Ce increasing from the analysis of C-f and G_p/ω-f measurement. Carrier compensation by the deep level traps causes high resistivity of Si:Ce film. From the XRD measurements, decrease of lattice parameter was observed in the high resistive samples. A high concentration of vacancies would result in formation of vacancy-vacancy and vacancy-Ce complexes. The appearance of deep level traps is attributed to the presence of these point-defect complexes.

References

[1] E. Płaczek-Popko and J. Szatkowski: J. Appl. Phys. **95** (2004) 1171.

[2] E. Płaczek-Popko, K. Sierański, J. Trzmiel, J. Szatkowski, and A. Nowak: phys. stat. sol. (c) **3** (2006) 1176.

[3] J. M. Wrobel, A. Gubański, E. Płaczek-Popko, J. Rezmer, and P. Becla: J. Appl. Phys. **103** (2008) 063720.

[4] H. Ennen, J. Schneider, G. Pomrenke, and A. Axmann: Appl. Phys. Lett. **43** (1983) 943.

[5] J. Olea, G. González-Díaz, D. Pastor, and I. Mártil : J. Phys. D: Appl. Phys. **42** (2009) 085110

[6] R. Kwo, M. Hong, A. R. Kortan, K. T. Queeney, Y. J. Chabal, J. P. Mannaerts, T. Boone, J. J. Krajewski, A. M. Sergent, and J. M. Rosamilia: Appl. Phys. Lett. **77** (2000) 130.

[7] J.J. Araisa, M. Cardenas, C. Falcaony, V. H. Mendez-Carcia, M. Lopez, and G. Cortrenas-Puente: J. Vac. Sci. Technol. A: **16** (1998) 3305.

[8] J.J. Araisa, M. A. Aguilar-Frutis, and C. Falcaony: J. Vac. Sci. Technol. B: **19** (2001) 2206.

[9] A. Dimoulas, G. Vellianitis, A. Travlos, V. Ioannou-Sougleridis, and A. G. Nassiopoulou : J. Appl. Phys. **92** (2002) 426.

[10] A. Dimoulas, A. Travlos, G. Vellianitis, N. Boukos, and K. Argyropoulps : J. Appl. Phys. **90** (2001) 4224.

[11] Nicollian & Brews: *MOS Physics and Technology* (Wiliey-Interscience, 2003)

[12] S. Libertino, S. Coffa, G. Franzó, and F. Priolo : J. Appl. Phys. **78** (1995) 3867.

[13] A. Cavallini, B. Fraboni, S. Pizzini, S. Binetti, S. Sanguinetti, L. Lazzarini, and G.

Salviati : J. Appl. Phys. **85** (1999) 1582.

[14] S. Libertino, S. Coffa, R. Mosca, and E. Gombia : J. Appl. Phys. **85** (1999) 2093.

[15] J. H. Evans-Freeman, and K. D. Vernon-Parry : Opt. Mater. **28** (2006) 802.

3

The effects of acceptor doping for the magnetic and magneto-transport properties of Si:Ce thin films

3.1　Intoroduction

In high temperature grown Si:Ce films with p-type conduction, various phenomena, such as ferromagnetic ordering, spinglass behavior, and/or giant magnetoresistance (MR), have been observed [1-4]. Employing a low temperature MBE growth, we successfully obtained uniformly Ce distributed Si:Ce films, which does not include precipitation of second phase such as Ce silicides. However these films exhibited n-type conduction and exhibited paramagnetic behavior in many cases [5]. It is indicated that hole plays an important role for the ferromagnetism of Si:Ce. As mentioned in chapter 2, LT-grown Si:Ce films with more than 0.09 at.% Ce are high resistive because of the strong compensation by the Ce-related deep level traps. For these LT-grown Si:Ce with uniform Ce distribution, it is important to know the effects of hole doping on the magnetic and magneto-transport properties.

In this chapter, in order to investigate the effect of the hole on the magnetic interaction, we fabricated homogenous Ce distributed low temperature (LT)-grown Si:Ce films with p-type conduction by means of codoping of Aluminum and Boron. The magnetization behavior and the magnetotransport properties of LT-grown p-type Si:Ce

films are reported.

3.2 Experimental

The boron co-doped Si:0.6at.%Ce epitaxial films were deposited by solid-source MBE method. The n-type Si(001) wafers with the carrier density below 1.0×10^{13} cm^{-3} were used as the substrates. The 100 nm thick Si:Ce,B were deposited after the growth of 30 nm thick Si buffer layer. The base pressure was below 1×10^{-9} torr and the growth temperature of Si:Ce,B was fixed at 610 °C. A 5 nm thick Si capping layer was grown at the same deposition temperature on the top of the Si:Ce,B films. The aluminum co-doped Si:0.6at.%Ce films were also deposited in the same process. For the growth of the Al-doped Si:Ce films, SOI (Si on insulator) (100) wafers were used as the substrates. The thickness of the top Si layer and SiO$_2$ layer of the SOI are 70 and 145 nm, respectively.

The surface morphology and the structure were evaluated by using reflection high-energy electron diffraction (RHEED) and atomic force microscopy (AFM). A superconducting quantum interference device (SQUID) was used for evaluating the magnetization behavior. For the electrical measurement, the Al electrode was deposited on the samples through a shadow mask after removal of native SiO$_2$. The electrical resistivity and the Hall effect were measured in the van der Pauw configuration at the measurement temperature from 2 to 300 K. For the magnetoresistance (MR) measurement, magnetic field is applied parallel to the current direction.

3.3　Results and Discussion

3.3.1　Crystallinity and magnetic properties of acceptor doped Si:Ce thin films

Low temperature growth enables the film to have a uniform distribution of Ce in epitaxial Si films without segregating the second phases or inhomogeneous Ce clustering. For all the films fabricated at these deposition conditions, no precipitation of second phase such as cerium silicide is recognized by *in situ* RHEED and *ex situ* XRD observations.

Figure 3-1 shows the magnetization (M-H) curve of LT(610 °C)-grown Al doped Si:0.6at.%Ce films and B doped Si:0.6at.%Ce films with different doping amount of Al and B, which is varied by doping cell temperature described in the figure. The measurement was carried out at 2 K and the magnetic field was applied parallel to the film surface. The samples without acceptor doping show two type magnetic behavior. One is paramagnetic and the other is ferromagnetic. At the present time, the origin of this difference has been under investigation. We added aluminum to the paramagnetic Si:Ce and added boron to the ferromagnetic Si:Ce. The samples with Al doping showed paramagnetic M-H curves. The M-H curves are well fitted to the Brillouin function. In the case of B doping to the ferromagnetic Si:Ce, ferromagnetic response disappear with increasing B concentration. The abrupt increase of magnetization in the low magnetic field decreases with increasing B concentration. The M-H curve of the heavily-B-doped film (B k-cell: 1450 °C) is well fitted to Brillouin function and exhibits paramagnetic behavior. In these samples, the magnetization values at 5 T are smaller than the magnetic moment of Ce, 2.54 μ_B. Therefore, the effective concentration of the Ce^{3+} ion
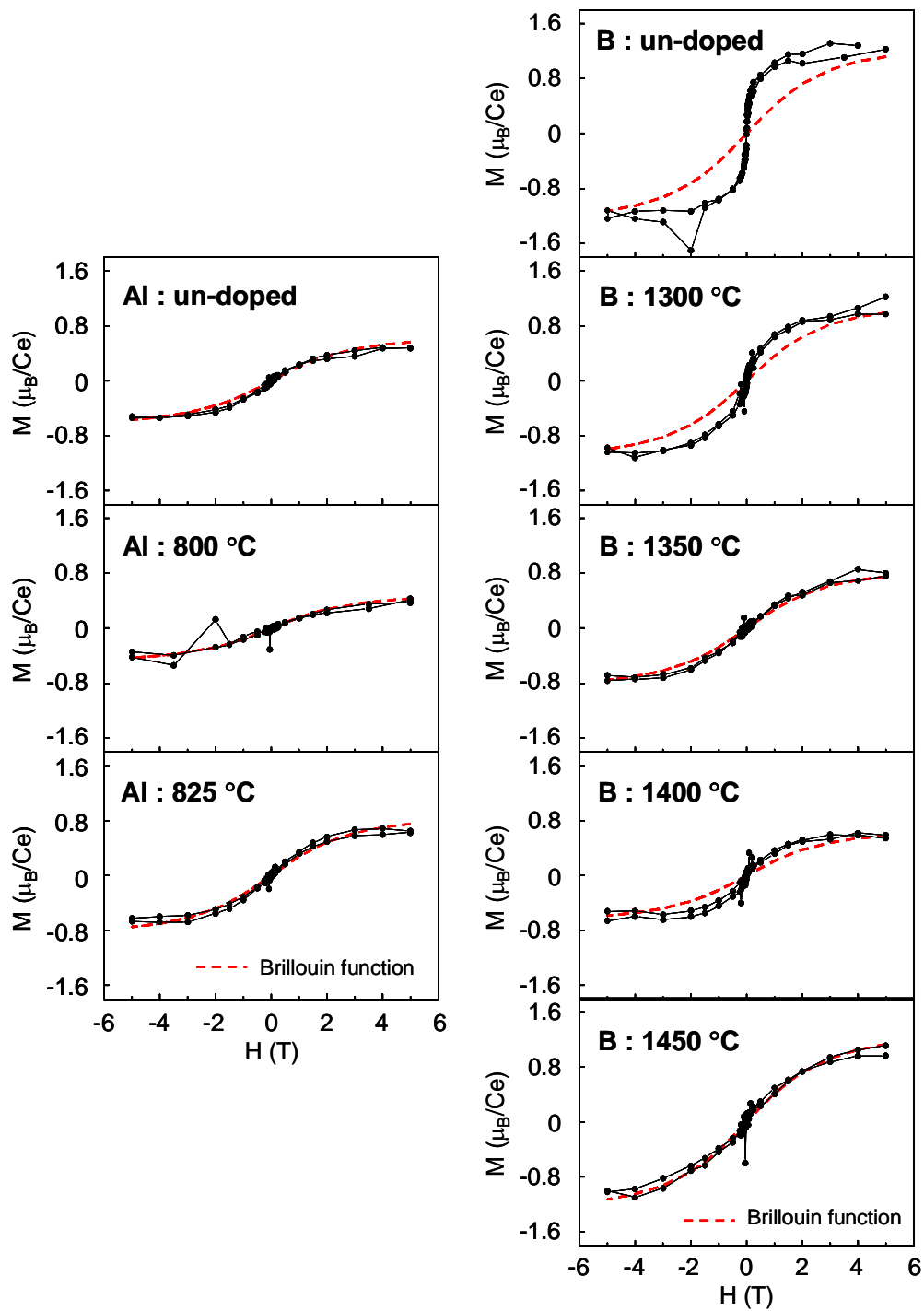
is considered to be low..

Fig. 3-1. Magnetization curves at 2 K for Si:0.6 at.%Ce with Al-doped and B-doped films grown at 610 °C.

3.3.2 Magneto-transport properties

3.3.2-1 Low hole density

The sample without acceptor doping showed n-type conduction due to the existence of point defects and showed parallel conduction with the substrate. The Si:Ce,B (B k-cell: 1300 °C) film also showed parallel conduction with the substrate. The Si:Ce,B (B k-cell: 1350 °C) film showed n-type conduction and the resistivity exponentially increases with decreasing temperature. In these samples, there are more electrons emitted from defects than holes emitted from boron. On the other hand, Al- and B-doped (B k-cell: 1400 and 1450 °C) samples showed p-type conduction with higher carrier concentration and lower resistance with increasing the k-cell temperature. Figure 3-2 (a) and (b) show the temperature dependence of the carrier concentration and resistivity of Al- and B- doped Si:0.6 at.%Ce thin films, respectively. The cell temperatures of Al and B were inserted in the figures. As shown in Fig. 3-2 (a), the carrier concentrations are almost constant in the temperature ranging from 80 to 300 K in all the samples. For the sample with lower carrier concentration (Al: $2.3 \times 10^{19} \text{cm}^{-3}$ at 80 K, B: $2.0 \times 10^{19} \text{cm}^{-3}$ at 80 K), the resistivity exponentially increases with decreasing the measurement temperature as shown in Fig. 3(b). The conduction mechanism of the sample is well fitted to a variable range hopping mechanism [6] expressed by

$$\sigma = A \exp\left\{-\left(T_0/T\right)^{1/2}\right\} \tag{3-1}$$

The sample showed positive MR at 2 K and the MR is also well fitted to

$$\ln\left(\frac{\rho(B)}{\rho(0)}\right) = t \frac{e^2 a^4}{\hbar^2} \left(\frac{T^*}{T}\right)^y B^2, \tag{3-2}$$

which is used as the MR in the variable range hopping region [7]. Figure 3-3 shows the

experimental MR and calculated results. In a low magnetic field region, negative MR, which is originated from a weak localization, is observed. In this sample, little carrier $4f$ spin interaction is supposed to be occurring in the magnetotransport behavior.
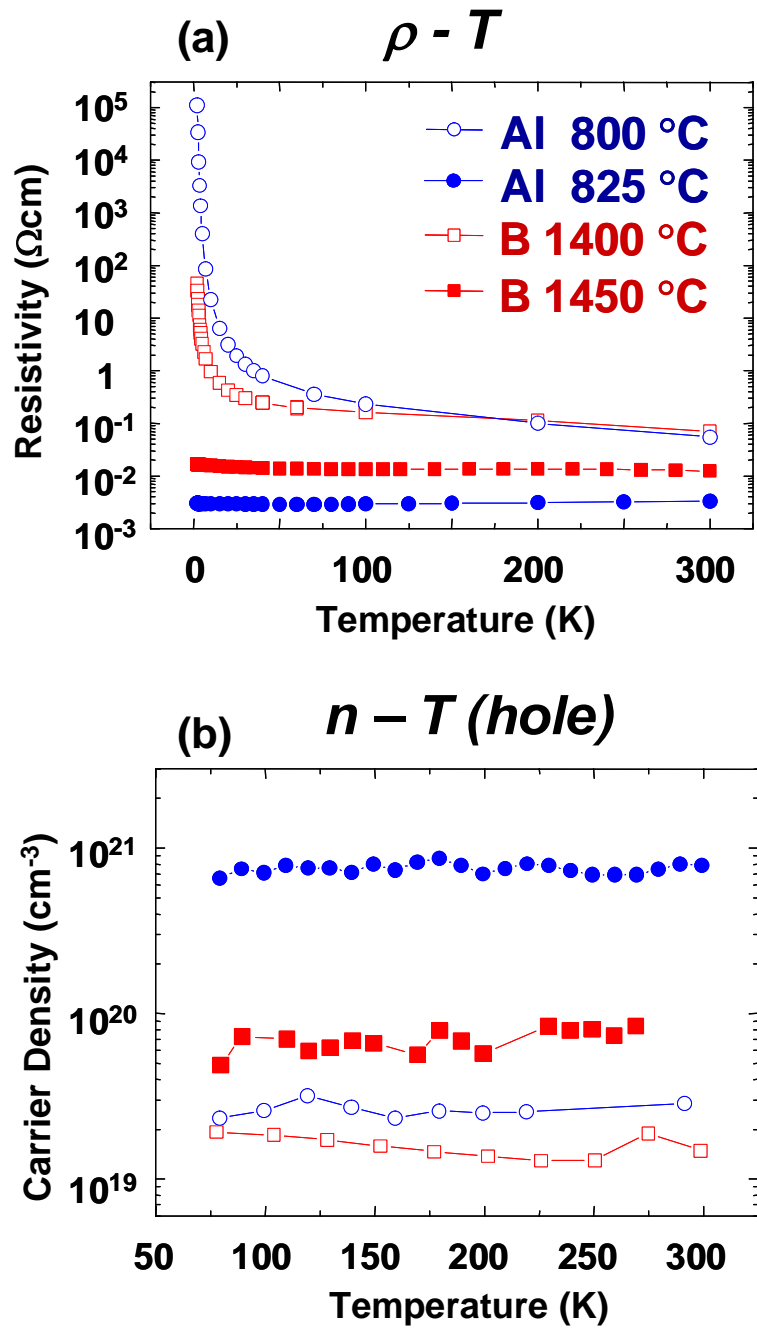
(a) ρ - T

(b) n – T (hole)

Fig. 3-2. Temperature dependence of resistivity (a) and carrier density (b) of Al-doped Si:0.6 at.%Ce and B-doped Si:0.6at.%Ce..
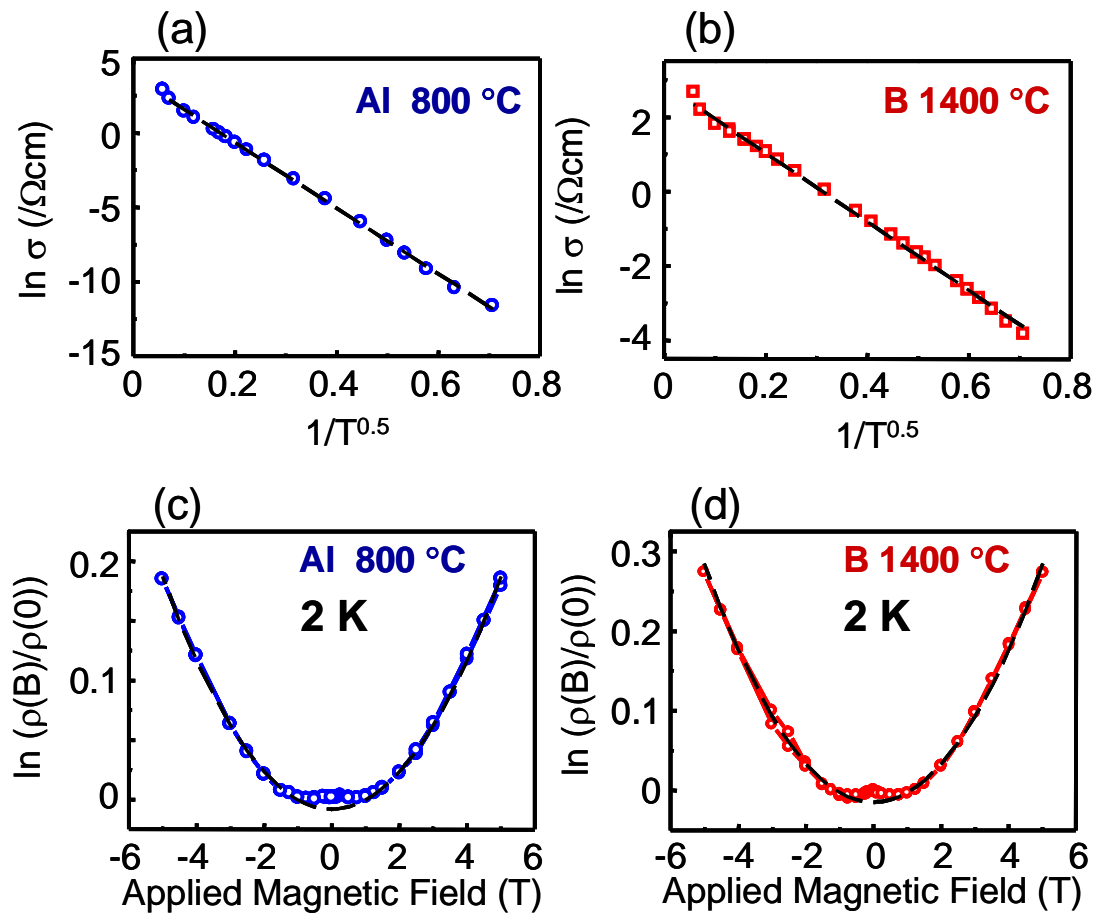
Fig. 3-3. Temperature dependence of conductance (a, b) and magnetic dependence of magnetoresistance (c, d) of low hole density films.

3.3.2-2   High hole density

The sample with higher carrier concentration (Al: 7×10^{20} cm^{-3} at 80 K, B: 5×10^{19} cm^{-3} at 80 K) shows a metallic conduction even at 2 K. The MR behavior of the sample measured at 2 K is shown in Fig. 3-4. The positive MR is observed, and it does not fit to the carrier hopping induced MR. In this case, therefore, the quantum corrections of *p-f* spin splitting on the disorder modified electron-electron interaction was applied for the analysis of the MR behavior [8,9]. The calculations of the conductivity and the positive MR were performed, according to the following equations:

$$\delta\sigma(T,h)_I = -\frac{e^2}{\hbar}\frac{\tilde{F}_\sigma}{4\pi^2}\sqrt{T/2D}\,g_3(h),$$

(3-3)

$$g_3(h) = \int_0^\infty d\Omega \frac{d^2}{d\Omega^2}\left[\Omega N(\Omega)\right]\left(\sqrt{\Omega+h}+\sqrt{\Omega-h}-2\sqrt{\Omega}\right),$$

(3-4)

$$h = \frac{g\mu_B H + x_{eff}\beta N_0 J B_J(T,H)}{k_B T},$$

(3-5)

βN_0 (*p-f* exchange interaction energy) and F_σ (the screening parameter for the Coulomb interaction) are used as fitting parameters. x_{eff} effective mole fraction of the magnetic ions is 0.0024 (Al-doped Si:Ce) and 0.0030 (B-doped Si:Ce) deduced from the experimental magnetization measurement. With considering not only Zeeman splitting but also *p-f* exchange interaction, we can fit this positive MR shown as the solid line in Fig. 3-5. The *p-f* interaction energy of Al- and B-doped Si:0.6at.%Ce thin films were calculated as 52 meV and 48 meV respectively, though they do not show any ferromagnetic nature. This is probably due to the existence of small effective Ce^{3+} concentration [5]. The MR measurement reveals the evidence of the interaction between hole and 4*f* spin for *p*-type Si:Ce films with uniformly Ce distribution, although they do not show ferromagnetic magnetization behavior. It is indicate that previously observed

ferromagnetism in Si:0.5at.%Ce films grown at 740 °C shown in chapter 1 is considered to be responsible for the localized high Ce concentration region in the film [2,4,10]. To enhance the ferromagnetic ordering, it should be required to design the Si:Ce structure so as to increase the amount of dissolved Ce in Si:Ce film. Superlattice structure or δ-doping of Ce is the promising structure for obtaining ferromagnetic nature in entire region of the Si:Ce film.

3.3.3   Mechanism of ferromagnetism in Si:Ce

Based on these results, the author propose a model of ferromagnetism in Si:Ce here.

When a Ce^{3+} ion is placed in a regular tetrahedral coordination (T_d symmetry), the spin-orbit interaction and the crystal filed split the $4f$ levels into a doublet (Γ_6, Γ_8) and a triplet (Γ_6, Γ_7, Γ_8) as shown in Fig. 3-6 [11]. On the substitutional Ce in Si, theoretical study has been worked [12] and have reported that if the $4f$ electron is treated as core electrons screened by the $5s$, $5p$ filled shells and $6s$, $5d$ valence orbitals, lower $4f$ levels ($^2F_{5/2}$) lie deep in the Si valence band. However this 'frozen $4f$' approximation seems not to be infallible, since photoemission measurements of verified experimentally that $4f$ orbitals of rare-earth elements would hybridize with the Si valence band [13].

In the theoretical study of a Si:Er system, Wan *et al* [14] treated the Er $4f$ orbitals as valence states in order to describe the electronic structures by taking into account the interactions between the impurity and the host Si. In the work of Wan *et al* [14], Er $4f$-like levels lie near the edge of the valence band. The reason is that the compression of the charges stored in the delocalized Er $6s$ and Er $5d$, due to the solid-state environment, increases the Coulomb interaction between $4f$ and external electrons, and

as a result the 4*f*-like states rise in energy to the point of overlapping the valence-band states while remaining localized.

In the case of Si:Ce system, it is also expected that the hybridization among Ce 4*f*, 5*d*, and 6*s* orbitals is responsible for the interaction between the Ce and Si host. From the results of the chapter 2, existence of the midgap states derived from complex defects is indicated on the LT-grown Si:Ce films. From the results of the chapter 3, it is indicated that ferromagnetic behavior in the LT-grown Si:Ce is suppressed by heavily doping of the shallow acceptor though it has the *p-f* exchange interaction. Based on these results, it is considered that the LT-grown Si:Ce have the energy band diagram as shown in Fig. 3-7. Donor states derived from the point defect is formed below the bottom of the conduction band and complex defect state acting as the trap site is formed around midgap. Ce 4*f* levels lie in the band gap near the edge of the valence band. As deposited LT-grown Si:Ce films is considered to have the energy band diagram as shown in Fig.3-7(a). This energy band shows paramagnetic nature. When the spin split of the 4*f* level is much larger than the presented split in Fig. 3-7(a), ferromagnetism would occur without acceptor doping such as B-undoped Si:0.6at.%Ce. Slightly acceptor doping lower the Fermi level position. The number of the up spin increases and the film becomes ferromagnetic (Fig. 3-7(b)). Further doping of the acceptor lower the Fermi level position up to below the 4*f* states. The number of the 4*f* electron decreases and ferromagnetic behavior is suppressed (Fig. 3-7(c)).

If the 4*f* levels lie deep in the valence band, *p-f* exchange Zener model is also considered the origin of the ferromagnetism. Zener first proposed a model of ferromagnetism driven by the exchange coupling of the carrier and the localized spins. According to that model, spin polarization of the localized spins leads to spin splitting

of the bands, which results in the lowering of the carrier energy [15]. The *p-d* exchange Zener model, which is expanded by Dietl [16], is extensively discussed in III-V group ferromagnetic DMSs such as (Ga,Mn)As, (In,Mn)As. The Mn concentration and carrier density are important in the ferromagnetic transition temperature. It is discussed that the ferromagnetism is mediated by delocalized or weakly localized holes in zinc-blend and wurzite diluted magnetic semiconductors. According to the *p-f* exchange Zener model, it is expected that acceptor doping enhance the ferromagnetic nature of the Si:Ce films. In fact, however, ferromagnetic behavior was suppressed by the acceptor doping. This experimental result contradicts the *p-f* exchange Zener model. The energy band picture as shown in Fig. 3-7 can well explain the experimental results. In the Fig. 3-7(b), although this band diagram indicates the metallic conduction in the impurity band, such a metallic conduction is not confirmed in the ferromagnetic Si:Ce films yet. In fact, hopping conduction between the localized states will occur with the carrier transport in the valence band or conduction band. The origin of the ferromagnetism in Si:Ce films is expected to be the double-exchange interaction mediated by *p-f* exchange interaction [17]. Partially occupied 4*f* state is also important for the ferromagnetism.
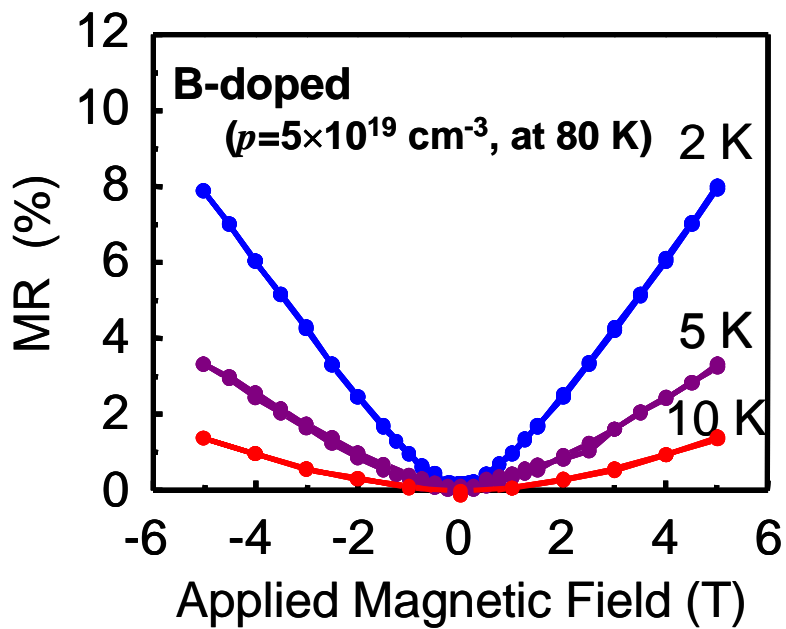
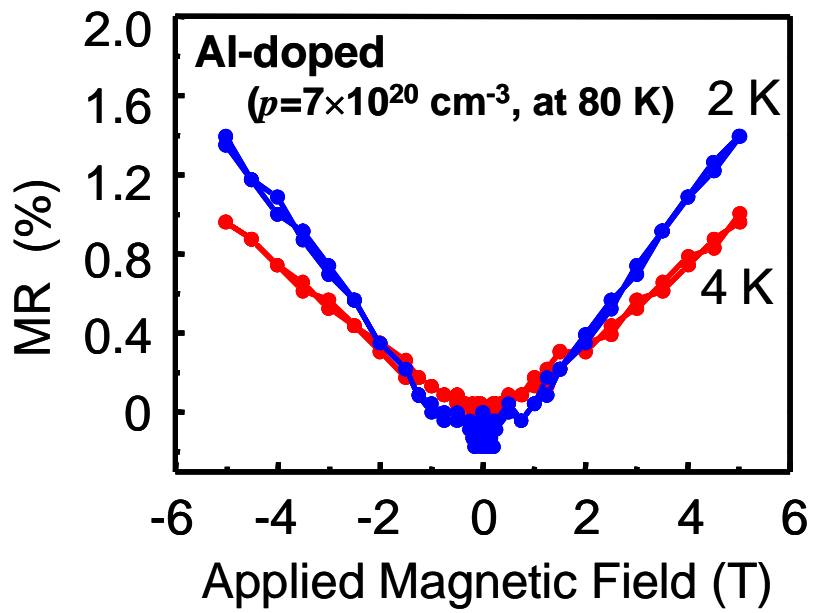Fig. 3-4. Magnetic field dependence of magnetoresistance of high hole
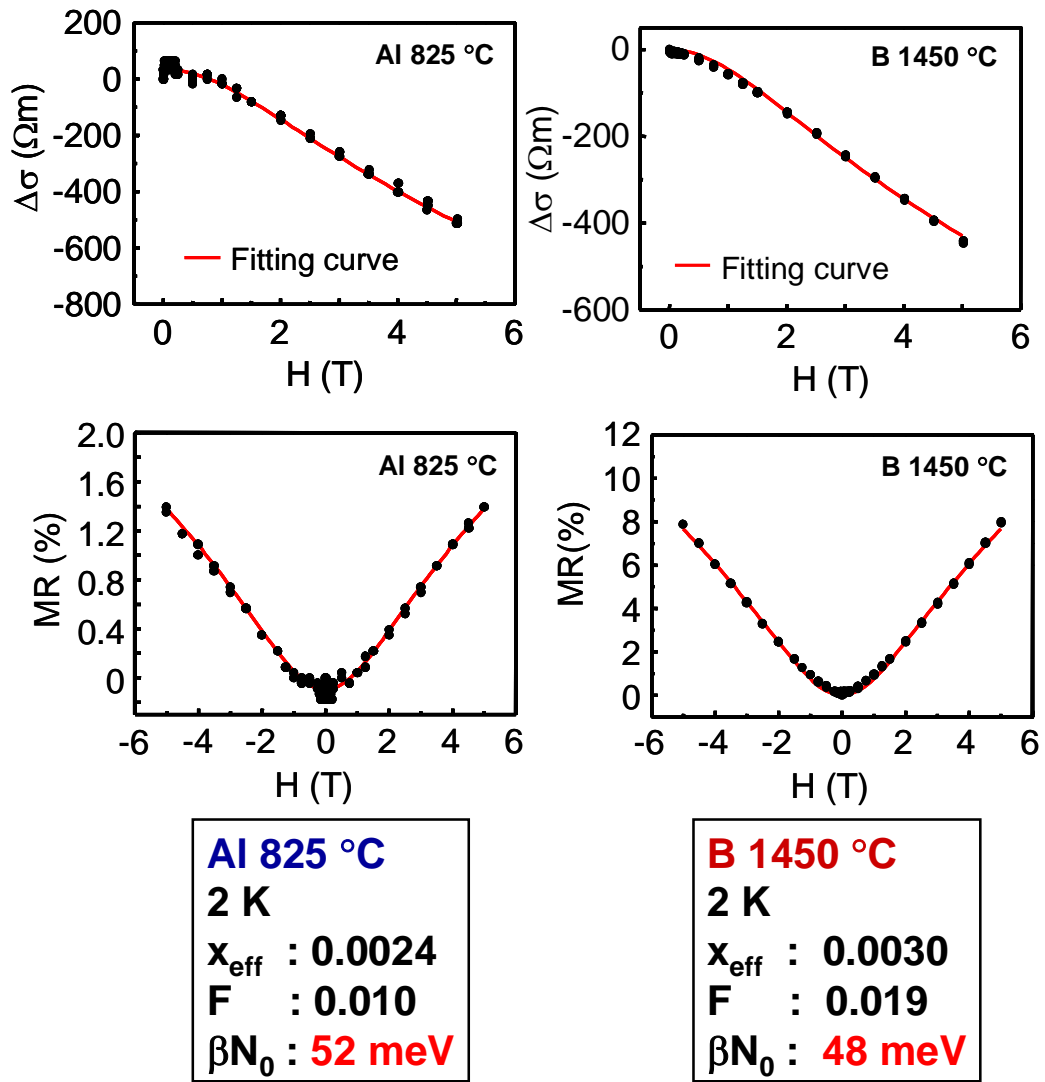density films.

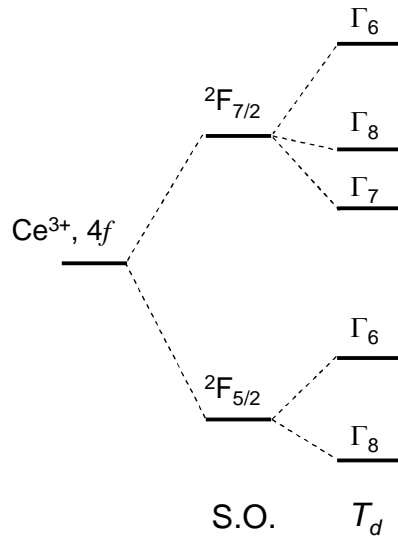Fig. 3-5.   Fitting result of MR at 2 K and the fitting parameter.

Fig. 3-6.   Crystal field and spin-orbit splitting of the $4f$ level of Ce^{3+} ion [Ref.11].
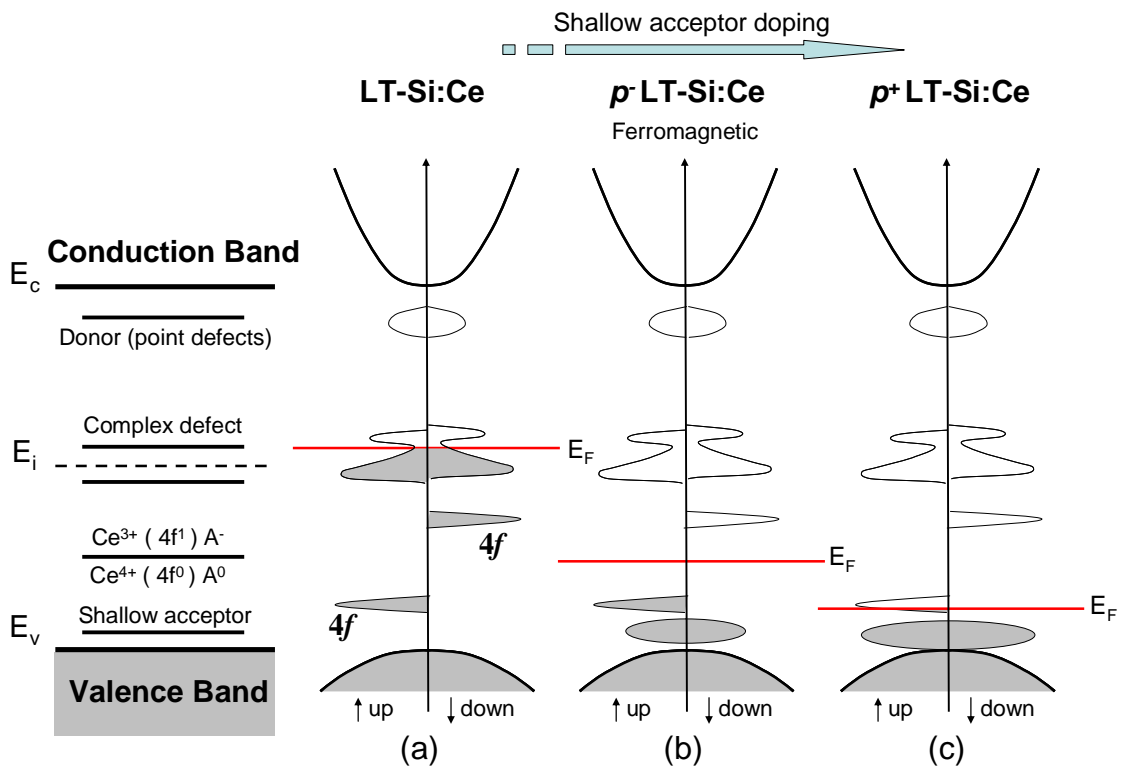

Fig. 3-7.   A schematic energy band diagram of LT-grown Si:Ce. Si:Ce without acceptor doping (a), with slightly acceptor doping (b), with heavily acceptor doping (c).

3.4　Conclusion

LT-grown p-type Si:Ce thin films were fabricated by means of acceptor doping without segregation of Ce silicide. The ferromagnetic magnetization behavior of the Si:Ce film was suppressed by the heavily acceptor doping and the acceptor-doped films show paramagnetic magnetization behavior. It is suggested that Ce ion is uniformly distributed and no high concentration region of Ce^{3+} ion is included. From the change of the magnetic properties, it is considered that Ce $4f$ levels lie in the Si band gap near the valence band edge. The film with metallic conduction shows distinct carrier-$4f$ spin exchange interaction by analyzing the MR behavior. The p-f interaction energy of the film is calculated as 52 meV (Al doped Si:Ce) and 48 meV (B doped Si:Ce), respectively. On the basis of this result, the hole plays an important role in the magnetic properties of the Ce-doped Si thin films. And it is also important for the ferromagnetism in Si:Ce that Fermi level lies in the $4f$ states.

References

[1] T. Yokota, N. Fujimura, and T. Ito: Appl. Phys. Lett. **81** (2002) 4023.

[2] T. Yokota, N. Fujimura, T. Wada, S. Hamasaki, and T. Ito: J. Appl. Phys. **91** (2002) 7905.

[3] T. Yokota, N. Fujimura, and T. Ito: J. Appl. Phys. **93** (2003) 4045.

[4] T. Yokota, N. Fujimura, T. Wada, S. Hamasaki, and T. Ito: J. Appl. Phys. **93** (2003) 7679.

[5] T. Terao, K. Fujii, D. Shindo, T. Yoshimura, and N. Fujimura: Jpn. J. Appl. Phys. **48** (2009) 033003.

[6] N. F. Mott, *Metal-Insulator Transitions*, 2nd ed. (Taylor & Francis, London, 1990).

[7] B. I. Shklovskii and A. L. Efros, *Electronic Properties of Doped Semiconductors* (Springer, Berlin, 1984).

[8] P. A. Lee and T. V. Ramakrishnan: Rev. Mod. Phys. **57** (1985) 287.

[9] Q. Xu, L. Hartmann, H. Schmidt, H. Hochmuth, M. Lorenz, D. Spemann, and M. Grundmann: Phys. Rev. B. **76** (2007) 134417.

[10] T. Terao, Y. Nishimura, D. Shindo, T. Yoshimura, A. Ashida, and N. Fujimura: J. Magn. Magn. Mater. **310** (2007) e726.

[11] T. Hoshina and S. Kuboniwa: J. Phys. Soc. Jpn. **31** (1971) 828.

[12] C. Delerue and M. Lannoo: Phys. Rev. Lett. **67** (1991) 3006.

[13] G. Rossi: Surf. Sci. Rep. **7** (1987) 1.

[14] J. Wan, Y. Ling, Q. Sun, and X. Wang: Phys. Rev. B. **58** (1998) 10415.

[15] C. Zener: Phys. Rev. **81** (1951) 440.

[16] T. Dietl : Phys. Rev. B. **63** (2001) 195205.

[17] H. Akai : Phys. Rev. Lett. **81** (1998) 3002.

4

The application of the ferroelectric thin film as the gate insulator

4.1   Intoroduction

By the heavily shallow acceptor co-doping to the LT-grown Si:Ce film, the film becomes metallic though LT-grwon Si:Ce itself is high resisitive because of the large trap site density at deep level. And it is revealed that a hole interacts with $4f$ electron. Meanwhile, the heavily shallow acceptor co-doped Si:Ce film shows paramagnetic M-H curve. Given these results, the band structure of Si:Ce as shown in Fig. 3-6 is proposed. By moving the Fermi level, the magnetic properties can be controlled.

For diluted magnetic semiconductor (DMS), control of the magnetism by the application of external electric fields to modulate the carrier concentration should be attractive phenomena. This is of course quite important for understanding the electric field effect for DMS, which shows carrier induced ferromagnetism because it enables the carrier modulation without changing the crystal structure. Although an electrical control of Curie temperature T_C of ferromagnetic semiconductor (In,Mn)As, (Ga,Mn)As have been reported [1,2], the change of T_C is about a few Kelvin. Since ferroelectric materials can supply large amount of charge with a small electric field and can use remanent polarization, it should be suitable as a gate insulator for studying such a field effect.

Generally, ferroelectric oxide needs high deposition temperature (700 ~ 1000 °C) for the film crystallization. This temperature is high for Si:Ce because precipitation of $CeSi_x$ occur. In this work, ferroelectric $YMnO_3$ film was used as a gate insulator. Since $YMnO_3$ shows ferroelectricity only along <0001>, it is quite important to grow with (0001) preferential orientation. Therefore, we adopted to fabricate bottom gate type metal–ferroelectric-DMS (MFS) structure to obtain the epitaxial (0001) $YMnO_3$ film with excellent ferroelectricity because the lattice mismatch between Si and $YMnO_3$ is 7.8 %. This structure should be effective to overcome the silicidation issue mentioned above.

This chapter describes the fabrication of bottom gate type MFS structure using Ce doped Si DMS and epitaxially grown ferroelectric $YMnO_3$ film and the dielectric properties of the MFS capacitor. We determined the induced charge density of the Si:Ce film by the ferroelectric $YMnO_3$ film from polarization measurements.

4.2   Experimental

$YMnO_3$ epitaxial films with a thickness of 100 nm were deposited on epitaxially grown (111) Pt/ (0001) sapphire substrates at 740 °C using pulsed laser deposition method. An ArF excimer laser (Lambda Physik) with a 193 nm wavelength was used for ablation. Details of the deposition have been reported elsewhere [3,4]. Ce doped Si films were deposited on the $YMnO_3$ epitaxial film by solid source molecular beam epitaxy method. Simultaneous evaporation of Si and Ce was carried out using high-temperature Knudsen cells. The pressure during deposition was kept below 2.4×10^{-9} Torr. The substrate temperature was measured by the thermocouple contacted to the

back of the substrate holder. The temperature was corrected using the pyrometer. A 2 nm-thick-Si capping layer were grown at 630 ℃ followed by the deposition of 25 nm-thick-Si:Ce layer. Deposition rate of Si was 30 nm/h. Surface morphology was evaluated by using *in-situ* reflective high-energy electron diffraction (RHEED) and *ex-situ* atomic force microscope (AFM). The structural analysis of the films was performed with *in-situ* RHEED and *ex-situ* high-resolution X-ray diffraction (HRXRD: Philips X'Pert-MRD) analysis. To evaluate the dielectric properties, Al electrodes were deposited on the DMS film through a shadow mask by rf magnetron sputtering method after removing the native SiO_2 by dipping in a 1 % HF solution for 1 min. Al electrode area was 1.5×10^{-4} cm^2. Capacitance-Voltage (*C-V*) and Capacitance-frequency (*C-f*) characteristics were measured at various DC bias in the 20 Hz to 1 MHz frequency range using a LCR meter (HP4284A). The leakage current was measured using a pico-ampere meter (4140B). Polarization measurements were performed using a Sawyer-Tower circuit.

4.3   Results and Discussion

4.3.1   YMnO₃ thin film

YMnO$_3$ films were epitaxially grown on epitaxial Pt/Sapphire. After depositing Pt top electrode, dielectric measurement was carried out. Figure 4-1 shows the *C-V* and *P-E* properties of Pt/YMnO$_3$/Pt MFM capacitor at room temperature. It shows a nonlinear increase of permittivity accompanying inversion of spontaneous polarization and shows the ferroelectric type hysteresis, indicating that this YMnO$_3$ film exhibits ferroelectricity.
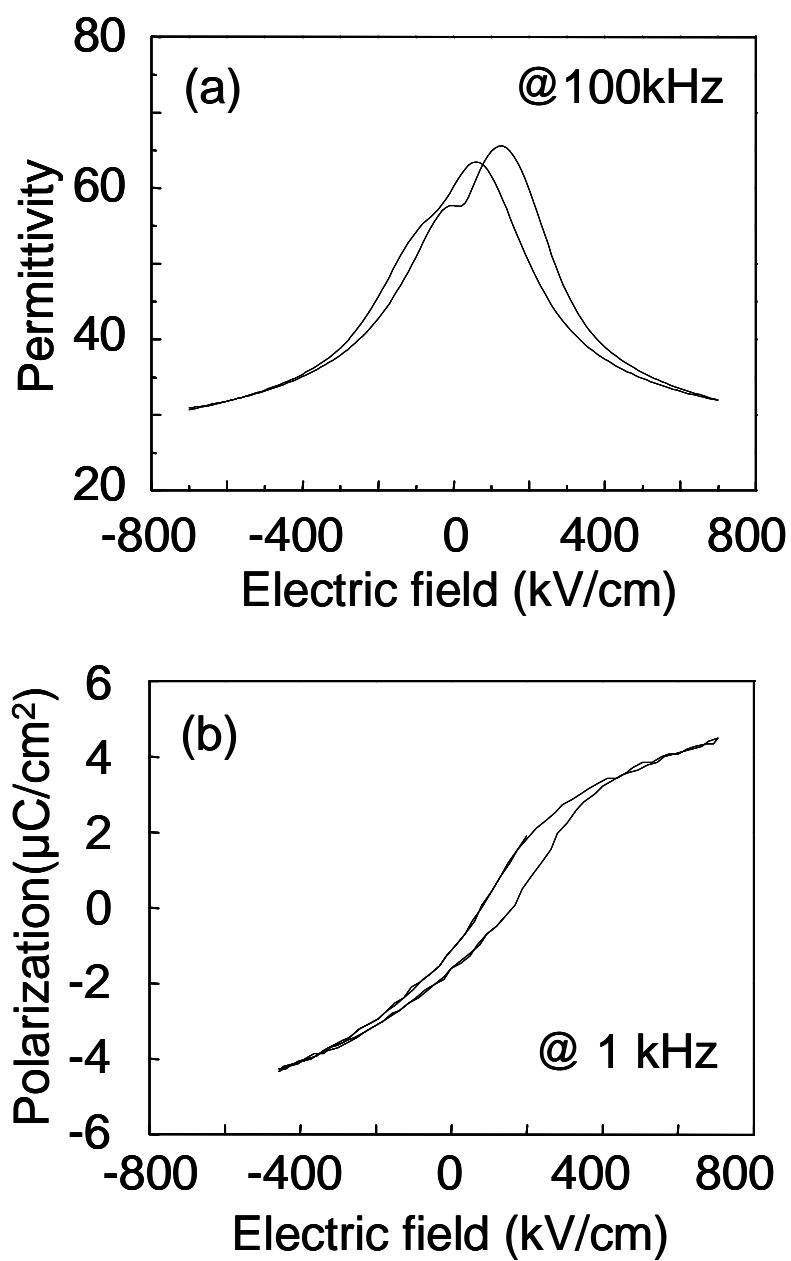
Fig. 4-1.   *C-V* (a) and *P-E* (b) characteristics of Pt/YMnO₃/Pt MFM
capacitor measured at room temperature.

4.3.2 Growth of Si:Ce thin film on the YMnO₃

The Si:Ce film with the Ce concentration of 2.9 at% was deposited on an epitaxial YMnO₃ film. Figure 4-2 (a) and (b) show the RHEED patterns of YMnO₃ film surface before Si:2.9at%Ce deposition and Si:2.9at%Ce film surface on the YMnO₃ film respectively. The RHEED pattern of the YMnO₃ surface shows a sharp streak indicating the excellent epitaxial film with a flat surface. Although the polycrystalline RHEED pattern is observed for the Si:Ce film, the structural analysis reveals that the crystal structure can be assigned to a diamond structure and no extra diffractions corresponding to the silicide are recognized.
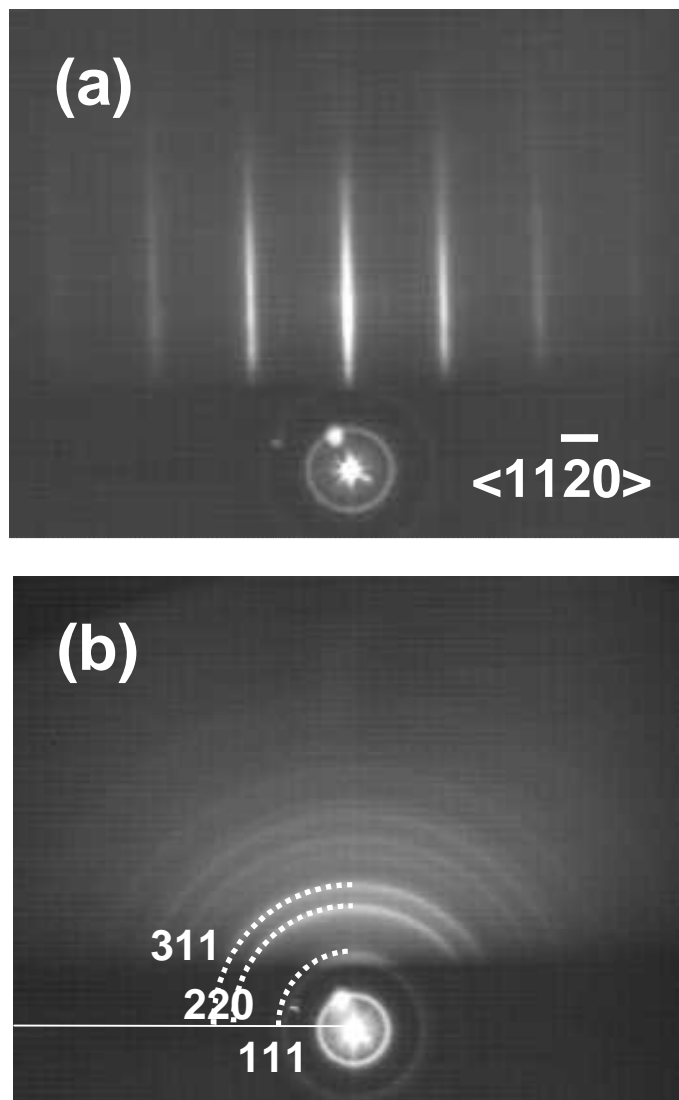
Fig. 4-2. RHEED patterns of YMnO₃ film surface before Si:Ce deposition
(a) and Si:Ce film surface after 25 nm deposition (b).

4.3.3 Dielectric properties of YMnO$_3$/Si:Ce heterointerface

Figure 4-3 shows the frequency dependence of *C-V* characteristics of the bottom gate type Al/poly-Si:Ce/YMnO$_3$/Pt/sapphire MFS capacitor. The capacitance at negative bias voltage is lower than that at positive bias voltage, which indicates that the carrier in the Si:Ce film is depleted at negative bias voltage, indicating that the Si:Ce film has *n*-type conduction. Despite the presence of the counter-clockwise hysteresis loop, that suggests switching of ferroelectric polarization, the frequency dependence of the *C-V* characteristic is also observed. As the frequency becomes lower, both the accumulation capacitance and depletion capacitance increase. *C-f* characteristic at the accumulation state is shown in Fig. 4-3. Large frequency dispersions of the capacitance and the dielectric loss are observed. When the charges are trapped at defects, the trapped charges act as space charge. The inhomogeneously induced space charge acts as polarization. When the frequency of ac signal is higher than the time constant of charging and discharging of the space charge, the space charge does not respond to the ac signal. When the frequency of ac signal is lower, the capacitance becomes higher because the space charge responds to the ac signal. This behavior is recognized in Fig. 4-3 and Fig. 4-4. It indicates that slow polarization caused by the space charge is generated. Therefore, not only ferroelectric polarization but also the slow polarization induce the charge in the Si:Ce film and affect the *C-V* characteristics. This means that charge density calculated from the *C-V* characteristics is not equal to that induced by ferroelectric YMnO$_3$ film.
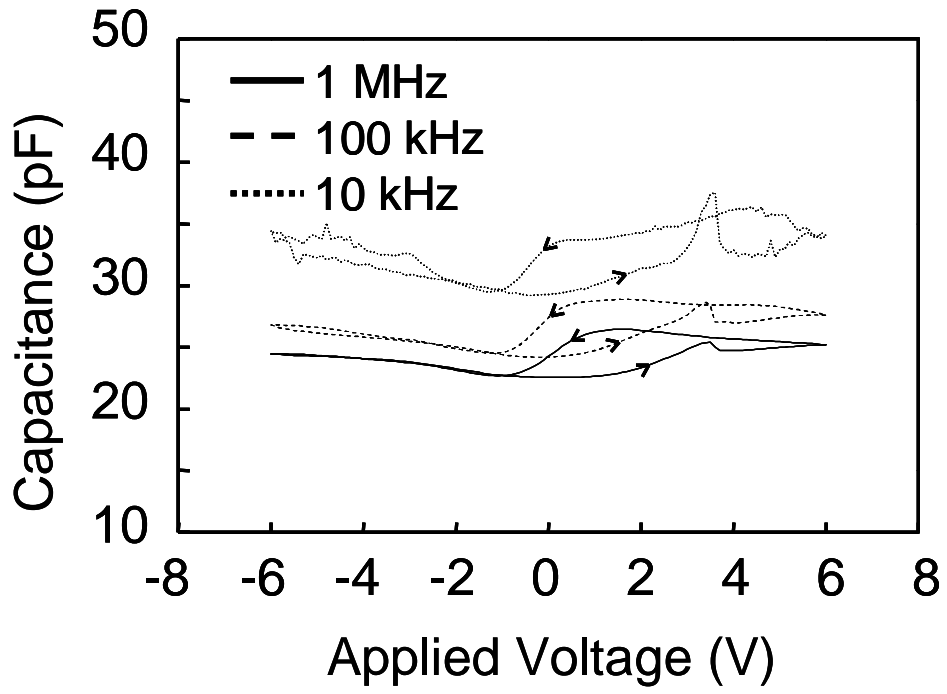
Fig. 4-3. Frequency dependence of *C-V* characteristics for the
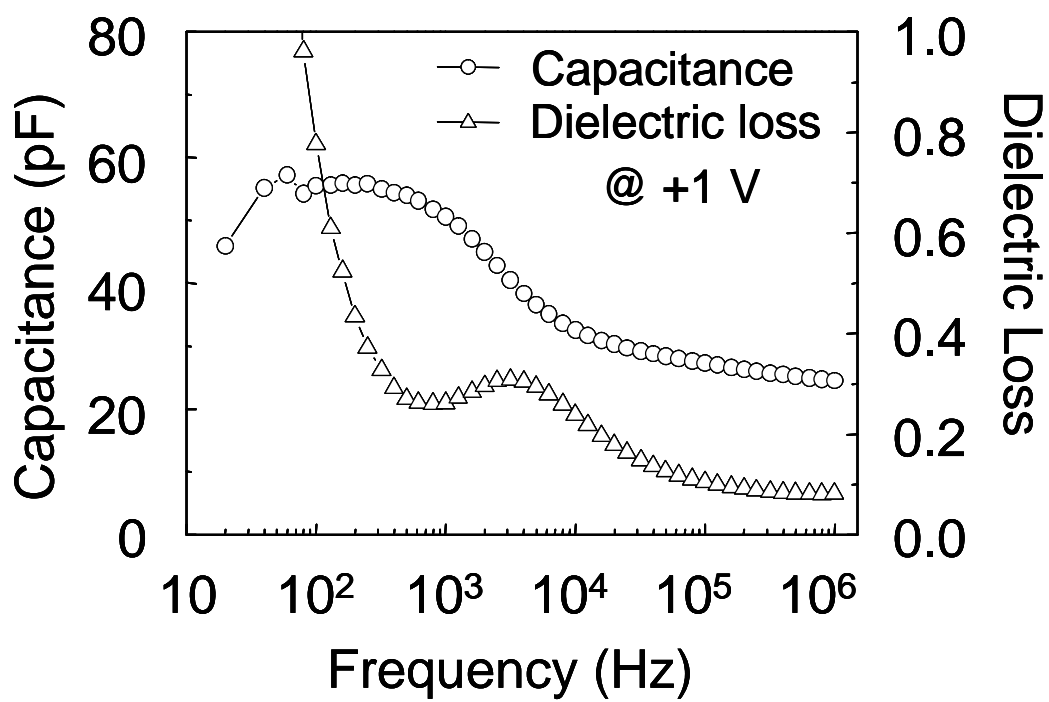Al/Si:Ce/YMnO$_3$/Pt capacitor.

Fig. 4-4. C-f characteristics of the Si:Ce/YMnO$_3$ capacitor at the accumulation state.

In order to distinguish between the ferroelectric polarization and the other polarizations, pulsed polarization measurements using positive up negative down (PUND) voltage pulse were performed. In the PUND measurements, positive voltage pulse is applied to the sample two times and then negative one is applied two times, and this sequence is repeated. From the transient behavior of the polarization for the voltage pulse, the effect of space charge can be deconvoluted from the switchable ferroelectric polarization.

Figure 4-5 shows the PUND voltage pattern and the polarization response. The used pulse width was 40 µsec. Square pulse of -3 V with 40 µs was applied before applying the first +3 V square pulse. As can be seen, the polarization response contains two components with different time constant. To characterize the time constant of the transient behavior of the polarization, the polarization response was fitted by Eq. (4-1) for charging region and Eq. (4-2) for discharging region,

$$P(t) = A_1 \left\{ 1 - \exp\left(-\frac{t}{\tau_1} \right) \right\} + A_2 \left\{ 1 - \exp\left(-\frac{t}{\tau_2} \right) \right\} \qquad (4\text{-}1)$$

$$P(t) = A_3 \exp\left(-\frac{t-w}{\tau_3} \right) + A_4 \exp\left(-\frac{t-w}{\tau_4} \right) + P_r \qquad (4\text{-}2)$$

where P is the polarization, t is the time, τ_i is the time constant, w is the pulse width, A_1, A_2 is the saturated value of polarization, A_3 and A_4 is the initial value of polarization, P_r is the remnant polarization.

The fitting result indicates that the magnitude of the fast polarization is 0.41 µC/cm^2 and the time constant of the slow polarization is 20 µs at the charging and 50 µs at the

discharging. It appears that the fast polarization is induced by the ferroelectricity of YMnO$_3$ film and the slow polarization is caused by the space charge which is accumulated at the interface of the trap.

In order to evaluate the only fast polarization without effect of other polarizations, *P-V* measurements at 100 kHz were performed. Figure 4-6 shows the results of the *P-V* measurements. The polarization at +3 V was 0.49 µC/cm^2 which is in good agreement with the result of the PUND measurement. In addition, the polarization at +6 V was 0.92 µC/cm^2 and at -6 V was -0.90 µC/cm^2. The capacitance calculated from the *P-V* characteristics is 24.1 pF, which is comparable with the accumulation capacitance on the *C-V* characteristics measured at high frequency.

Although the polarization induced by the YMnO$_3$ film is observed in the PUND and *P-V* measurement, the ferroelectric behavior such as remnant polarization is not recognized. This indicates that the voltage is not applied effectively to the YMnO$_3$ film due to the formation of the low dielectric layer or that the ferroelectricity of the YMnO$_3$ film is deteriorated during the deposition of the Si:Ce film.

However, for example, in the *n*-type Si with a carrier concentration of 10^{18} cm^{-3}, the surface charge density around -0.90 µC/cm^2 is large enough to form an inversion layer. Therefore, by improving the interfacial properties and reducing the leakage current of the gate ferroelectric layer, it can be expected that modulation of not only carrier concentration but also carrier type of DMS Si:Ce thin film.
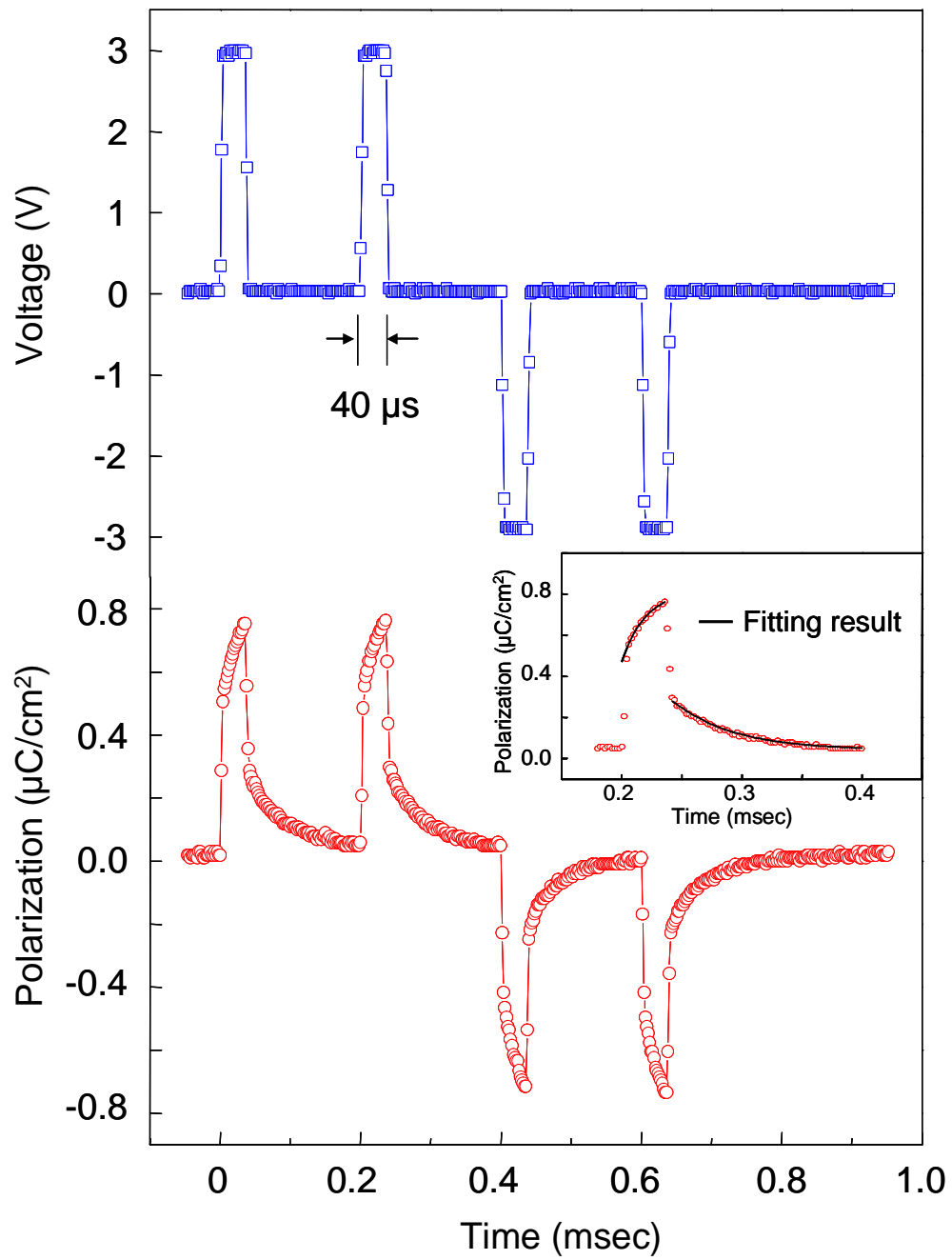
Fig. 4-5.   PUND voltage pattern (a) and the polarization response (b).
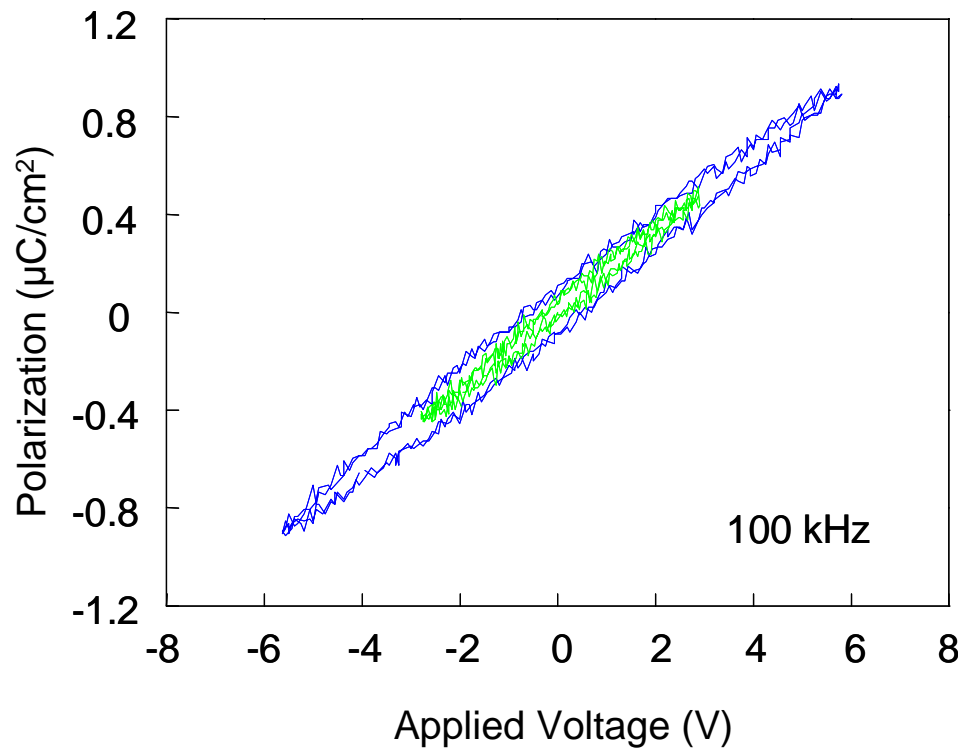The inset is the fitting result.

Fig. 4-6.   P-V characteristics of Al/Si:Ce/YMnO$_3$/Pt capacitor at 100 kHz under the bias voltage of ±3 V (thick line) and .±6 V (thin plot).

4.4　Conclusion

Although it was a polycrystalline film, Si:2.9at%Ce film without silicide precipitation was successfully obtained on epitaxial grown ferroelectric $YMnO_3$.

The dielectric properties of bottom gate type $Pt/YMnO_3/Si:2.9at\%Ce/Al$ MFS structure were investigated. Although the capacitance shows frequency dispersion, the capacitor exhibits a ferroelectric type C-V hysteresis loop. Detailed dielectric analysis revealed that the C-V hysteresis was caused by both ferroelectricity and space charge. From the P-V measurements at 100 kHz, although ferroelectric behaviors such as remnant polarization and saturation of polarization were not recognized, the measured polarization value originated from ferroelectric $YMnO_3$ was enough to obtain the carrier inversion of Si.

References

[1] H. Ohno, D. Chiba, F. Matsukura, T. Omiya, E. Abe, T. Dietl, Y. Ohno and K. Ohtani: Nature (London) **408** (2000) 944.

[2] D. Chiba, F. Matsukura, and H. Ohno: Appl. Phys. Lett. **89** (2006) 162505.

[3] K. Maeda, N. Shigemitsu, T. Yoshimura and N. Fujimura: Trans. Mater. Res. Soc. Jpn. **31** (2006) 185

[4] N. Shigemitsu, H. Sakata, D. Ito, T. Yoshimura, A. Ashida and N. Fujimura: Jpn. J. Appl. Phys. **43** (2004) 6613.

5

Heavily doping of Ce atom into Si

5.1 Intoroduction

For obtaining the ferromagnetic Si:Ce film, both (1) proper Fermi level position and (2) high Ce concentration region should be required. For making the high Ce concentration region, a few methods such as delta doping and superlattice structure can use. A surface reconstruction also has potential to realize a heavily doping of impurity.

The interactions between RE metals and Si at the Si surface have been extensively studied in surface physics, with RE silicide formation receiving the most attention (e.g., Ref. 1 and references therein). Recently, considerable effort has also been devoted to better understanding RE-induced reconstruction on Si(001) surfaces, which precedes silicide formation in the coverage regime from submonolayers up to a few monolayers (MLs). Ordered two-dimensional (2D) reconstructions are important because they are possibly key precursor states for silicide growth. Scanning tunneling microscopy (STM) and low-energy electron diffraction (LEED) studies have revealed the growth of 2D reconstructions on the Si(001) substrate: 3×2 for Sm [2], 2×3/2×4 and 2×6 for Yb and Nd [3,4], 2×4 and 2×7 for Gd, Dy and Ho [5,6], and 2×3, c(4×2), 4×2, 5×2 and c(5×4) for Er [7,8]. These 2D reconstructions of Si(001) are often energetically stable. Thus, structures are expected to enable high doping of impurities with large size in Si [9].

In the case of Ce on Si(001), although silicides formation has been reported [10,11], observation of a surface reconstruction induced by Ce atoms has not been reported. Therefore, the surface reconstruction should be quite important not only for understanding the surface physics but also for obtaining high Ce concentrations without forming Ce silicides.

In this study, we examined the reconstructed surface structure of Si:Ce thin films by *in situ* reflection high-energy electron diffraction (RHEED) analysis. We found a new reconstructed surface structure induced by Ce. This chapter describes the new Ce-induced reconstructed surface structure and the formation process.

5.2   Experimental

Si:Ce epitaxial films were deposited by solid source MBE at a base pressure of the order of 10^{-10} torr. SOI (Si on insulator) (001) wafers made by Smart-Cut method (SOITEC, France) were used as substrates. The substrate was chemically cleaned with SemicoClean 23 (Furuuchi Chemical). After immersion in 1% HF solution for 3 min, the substrate was inserted into an ultrahigh-vacuum MBE chamber. The sample was carefully outgassed at 600 °C and β-SiC was intentionally formed at 830 °C to fix carbon at the interface between the Si buffer layer and the substrate. After growing the 30-nm-thick Si buffer layer at 580 °C, the substrate was then annealed at 750 °C in order to form a step and terrace surface structure. Prepared surface of the Si buffer layer exhibited the double-domain structure of 2×1 and 1×2 reconstructions. A 50-nm-thick Si:Ce layer was grown on the Si buffer layer in the deposition temperature range from 550 to 650 °C. For the deposition of the Si:Ce layer, Si and Ce were simultaneously

evaporated by using high-temperature Knudsen cells. A 5-nm-thick Si capping layer was eventually grown at the same temperature as that of the Si:Ce layer. The deposition rate of Si was fixed at 36 nm/h. The Ce concentration of the films was varied from 0.4 to 6.8 at.% by adjusting the deposition rate of Ce. The substrate temperature was measured with a thermocouple and pyrometer.

Surface morphology and structure were evaluated by *in situ* RHEED. The RHEED measurements were performed at an incident electron energy of 30 keV with the incident angle of around 1.0° along [110] azimuth. The composition of the films was evaluated by electron probe microanalysis (EPMA) and high-resolution Rutherford backscattering spectrometry (HR-RBS).

5.3   Results and Discussion

5.3.1   Ce-induced novel surface reconstruction of Si(001)

Figure 5-1 shows the *in situ* RHEED patterns of Si:Ce thin films grown at 600 °C with the Ce concentrations of 0.4 (a and b), 1.1 (c–f) and 4.5 at.% (g–j) respectively. The thickness of the film when the RHEED pattern was taken is indicated in each figure. Incident direction of the electron beam was parallel to [110] direction. The film doped with 0.4 at.% Ce shows a 2×1 reconstructed structure throughout the growth at thicknesses below 50 nm. In the film doped with 1.1 at.% Ce, although the 2×1 surface structure is recognized at thicknesses below 6 nm, the reconstructed surface structure changed from 2×1 to a new structure having a three-fold periodicity at the thickness around 12 nm,. The same three-fold periodicity is also observed when the electron beam

incidents along [1-10] azimuth (90 degree rotated position). Along [100] direction (45 degree rotated position), 1×1 structure was observed. Si surface has a double-domained 2×1 surface before Si:Ce deposition, this three-fold periodicity is likely to be responsible for the double-domained 3×1 reconstruction. In this case, however, Ce ion should exist at next-site neighbor, which makes the surface stress larger. The 3×3 reconstruction with anti-phase domain structure, 3×3 with short range ordered structure or 3×random structure is also the candidate for the three-fold periodicity on the Si double-domained 2×1 reconstruction. We have not clarify the two dimensional surface reconstructed structure of above 3 type structure by using the 1st ordered ring in RHEED pattern, or spot diffraction in 1/3 ordered ring. LEED analysis or Atomic scale analysis such as STM is the way to make sure the surface structure.. However, all our samples have Si layer with 5 nm on the top of Si:Ce. Therefore, it is quite difficult to analyze the surface structure in atomic level. In this paper, therefore, we refer to this three-fold periodicity as the reconstructed 3× surface structure.

The 3× surface remained until the thickness of 24 nm and then the 2×1 surface structure appears again at 30 nm. The 2×1 surface re-changed to 3× when the thickness reached 42 nm. As the Ce concentration become higher, the surface become rougher. In the case of the film with 4.5 at.% Ce, the 3× surface appears at the thickness of 1.8 nm, which is thinner compared to that of the film with lower Ce concentration. The surface changes to 1×1 structure and the roughness is getting poorer probably due to the Ce concentration is too high to keep two dimensional growth with smooth surface.

The change in the surface structure with respect to thickness and Ce concentration is summarized in Fig. 5-2. All the films had the 2×1 surface structure before Si:Ce deposition. Figure 5-2 (a) shows the dependence on thickness and Ce concentration of

0.4 at.%   1.1 at.%   4.5 at.%

a 6 nm

b 50 nm

c 6 nm

d 12 nm

e 30 nm

f 50 nm

g 0.6 nm
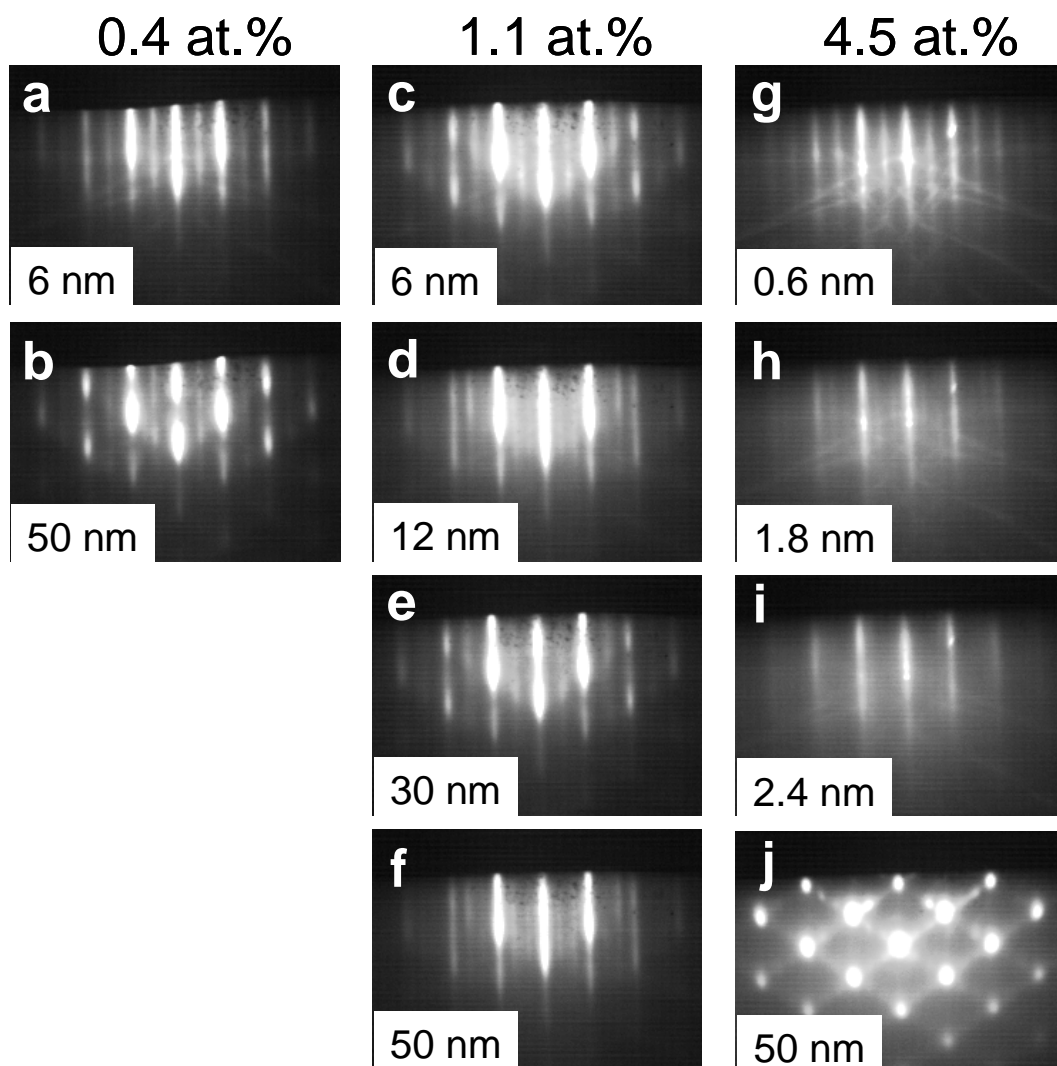
h 1.8 nm

i 2.4 nm

j 50 nm

Fig. 5-1.   RHEED pattern of Si:Ce thin films grown at 600 °C for Ce concentrations of 0.4 at.% (a, b), 1.1 at.% (c–f) and 4.5 at.% (g–j), respectively. Incident direction of the electron beam was parallel to [110] direction. Si:Ce film thicknesses when the RHEED pattern was taken are also shown.

RHEED pattern for Si:Ce films grown at 550 °C. In the case of the films with 0 and 0.4 at.% Ce, the 2×1 surface structure directly changes to spotty pattern, due to the 3D film growth. For films doped with 1.1 at.% Ce, the 2×1 surface structure does not change to the spotty pattern but rather to the 1×1 surface structure. This 1×1 surface structure remained until a thickness of 50 nm. The 3× surface structure is found in the films doped with 2.8 and 4.5 at.% Ce. The 3× surface structure changes to a spotty pattern though the 1×1 surface structure. When the Ce concentration is higher than 6.8 at.%, the 2×1 surface structure changes to the 1×1 surface structure without forming the 3× structure, and then changes to the spotty pattern. The process window for obtaining the 3× surface for films grown at 550 °C is narrower than that for films grown at 600 and 650 °C.

When the growth are done at 600 or 650 °C (Fig. 5-2 (b) or (c), respectively), the 3× surface structure is found for all films with Ce concentration greater than 1.1 at.%. At 600 °C, the film without Ce doping shows a sharp 2×1 streak throughout the growth and has a flat surface. In the case of the film with 0.4 at.% Ce, 2×1 surface structure remains until a thickness of 50 nm, although the diffraction pattern is slightly spotted. In films doped with 1.1 at.% Ce, the 2×1 surface structure changes to the 3× surface structure; the 2×1 surface structure then reformed, followed by the re-emergence of the 3× surface structure. The same 3× → 2×1 transition is observed in the film doped with 2.8 at.% Ce. This 2×1 surface structure changes to the spotty pattern because of the 3D film growth. Meanwhile, when the Ce concentration is higher than 4.5 at.%, the 3× surface structure changes not to the 2×1 structure but rather to the 1×1 structure, and then changes to the spotty pattern. At 650 °C, the critical thickness at which the 3× surface structure appears is almost the same as in the case of growth at 600 °C in the

films doped with 2.8 at.% Ce and higher. Below 2.8 at.%, the critical thickness is different with the case of growth at 600 and 550 °C. The 1×1 surface structure is not observed and the 3× surface changes directly to the spotty pattern. The 3× streak pattern of the film grown at 650 °C is sharper and clearer than the others. For the films with 0 and 0.4 at.% Ce, the 2×1 surface structure changes to the spotty pattern, suggesting the generation of 3D film growth. From these results, we found the following trend for the emergence of the 3× surface structure. At all observed growth temperatures, no films doped with 0.4 at.% Ce exhibited the 3× surface structure below thickness of 50 nm. As the Ce concentration was increased, the 3× surface appeared at thinner film thickness. When the growth temperature was low, the 1×1 surface appeared instead of the 3× surface. These results indicate that the 3× surface structure requires a certain amount of Ce atoms to form the structure, as well as sufficient heating and incubation time. We also examined whether 3× surface appears, when only Ce is deposited. Although the 3× pattern was recognized, the emergence of the 3× surface was poorly-reproducible.
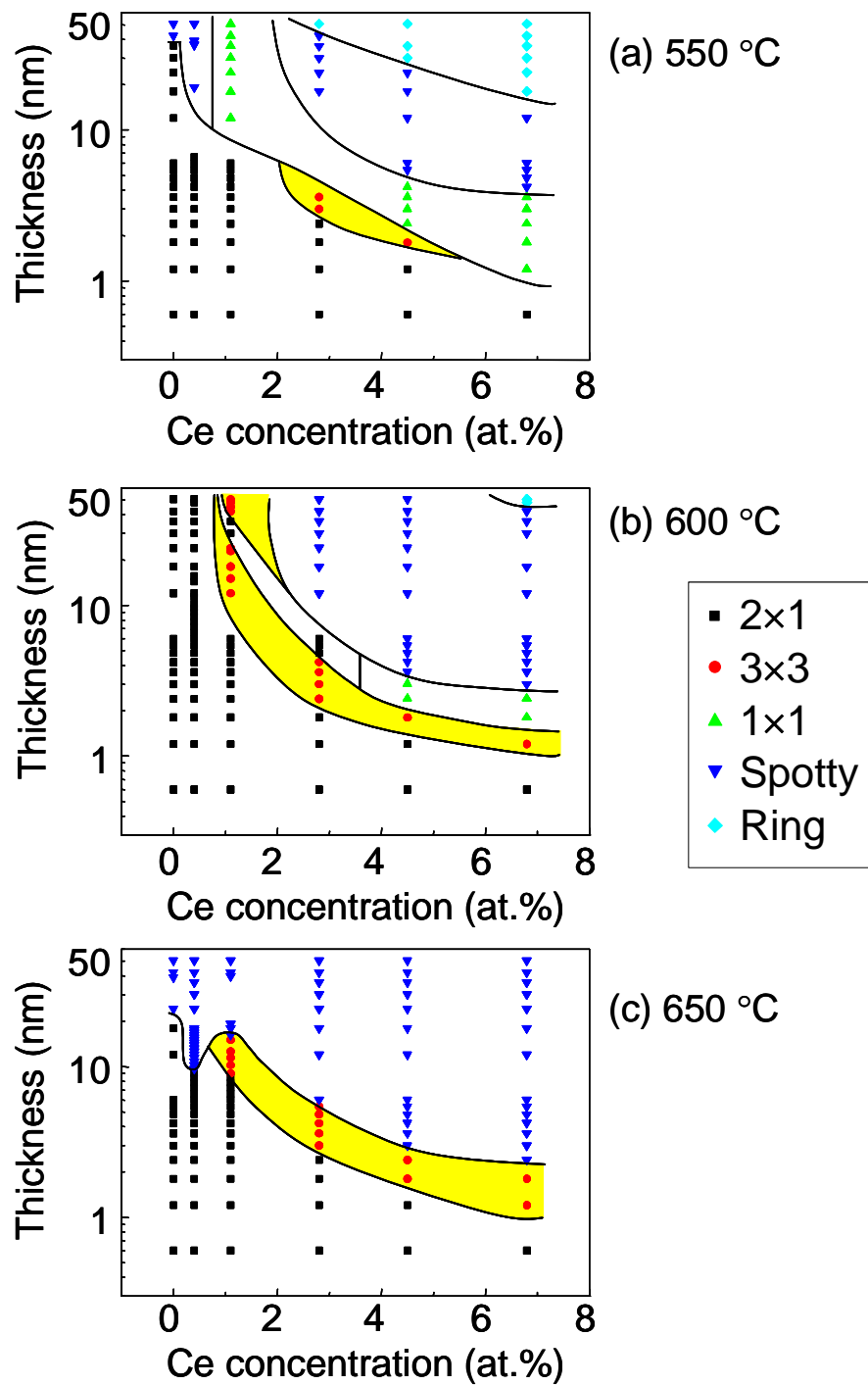
Fig. 5-2. Ce concentration dependence of RHEED patterns for Si:Ce films grown at 550 °C (a), 600 °C (b) and 650 °C (c). Solid lines indicate the boundary of each structure.

5.3.2 Depth profile of Ce atoms

Based on these experimental results, the diffusion to the surface of Ce atoms, the covalent radius of which is larger than that of Si, appears to play an important role in the formation of the 3× surface structure. For the Si film doped with 1.1 at.% Ce grown at 600 °C, the 3× → 2×1 → 3× transition is observed. To confirm whether the 3× surface structure remains in the film or not, the depth profile of Ce atoms in the films were investigated by HR-RBS analyses. HR-RBS analyses were carried out for the Si films doped with 1.1 at.% Ce deposited at 550 and 600 °C, as shown in Fig. 5-3 and Fig. 5-4. Arrows in Fig. 5-4(b) indicate where the reconstructed 3× surface structure appeared. In the case of the sample deposited at 550 °C, for which the 3× structure was not observed, little variation in the distribution of Ce atoms was observed. For the sample deposited at 600 °C, on the other hand, marked variation in the distribution of Ce atoms was found, and the high Ce concentration region corresponds to the formation of the 3× structure indicated with arrows. Therefore, Ce atoms diffused to the film surface during deposition, probably due to stress relaxation originating from the difference of the covalent radius of Ce and the Si [12,13]. Once the 3× structure is formed, the structure remains in the film probably because it is stable.

If the reconstructed 3× surface structure originates from the periodic arrangement of Ce atoms on the surface, the simplest hypothetical atomic arrangement is Si-Si-Ce-Si-Si-Ce, that is, three-fold periodicity of Si and Ce. In this case, if the reconstructions is 3×1 structure, the Ce concentration at the surface should be 33.3 at.%. In the case of the 3×3 structure, the Ce concentration at the surface should be 11.1 at.%. As mentioned above, although we have not solved the two dimensional surface structure, the candidates are as follows, 3×3 with anti-domain structure, 3×3 (short range ordered

structure), 3×random or 3×1 double domain structure. As the driving force of this periodic structure should be stress relief, the direction of this three-fold periodicity will be parallel to the dimer row. Perpendicular to the dimer row, the probability that Ce stays next to the Ce which makes 3×1 structure is low.

In either way, the 3× structure appears at much lower Ce concentration than that calculated using above atomic arrangement, suggesting that Ce diffuses to the surface until the surface Ce concentration reached 11.1 or 33.3 at.% locally. The maximum Ce concentration measured by HR-RBS shown in Fig. 5-4(b) was 1.5 at.% and it was lower than 11.1 and 33.3 at.%. It is considered that the 3× structure is formed locally on the surface, not on the whole surface.

We note that the high Ce concentration region corresponds well to the formation of the 3× structure, as shown in Fig. 5-4(b). In this study, although the precise reconstructed structure of the 3× surface was not determined by use of the double-domain 2×1 Si surface, this 3× surface can realize to make the high Ce concentration region on the Si:Ce film surface because of the three-fold periodic atomic arrangement. From the magnetization measurement by SQUID of the Si film doped with 1.1 at.% Ce grown at 600 °C, ferromagnetic magnetization behavior is observed even at 300 K. Although the films showing 3× surface structure does not always have the ferromagnetic nature, it is considered that high Ce concentration region is made in the film. If we can confine the 3× structure in the Si film more successfully, high Ce concentration region can be stably obtained [9]. This reconstructed surface with high Ce concentration should be available as a new technique to obtain a diluted magnetic semiconductor with high magnetic element. Low-dimensional systems such as reconstructed 2D structures are of great interest for both fundamental science and

nanotechnology. Recently, Yaji *et al.* have reported on the large Rashba spin splitting of a metallic surface-state band on a Ge(111) surface induced by a Pb monolayer [14]. This is an especially interesting result for developing semiconductor spintronic devices. Precise control of the surface reconstruction will enable novel $4f$ electron related phenomena to be found in the low-dimensional system.
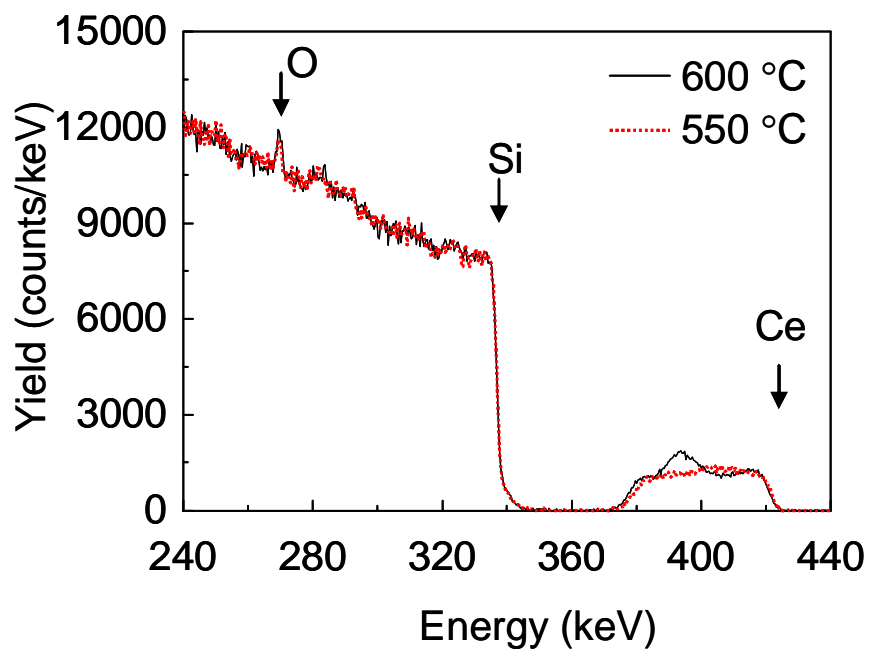
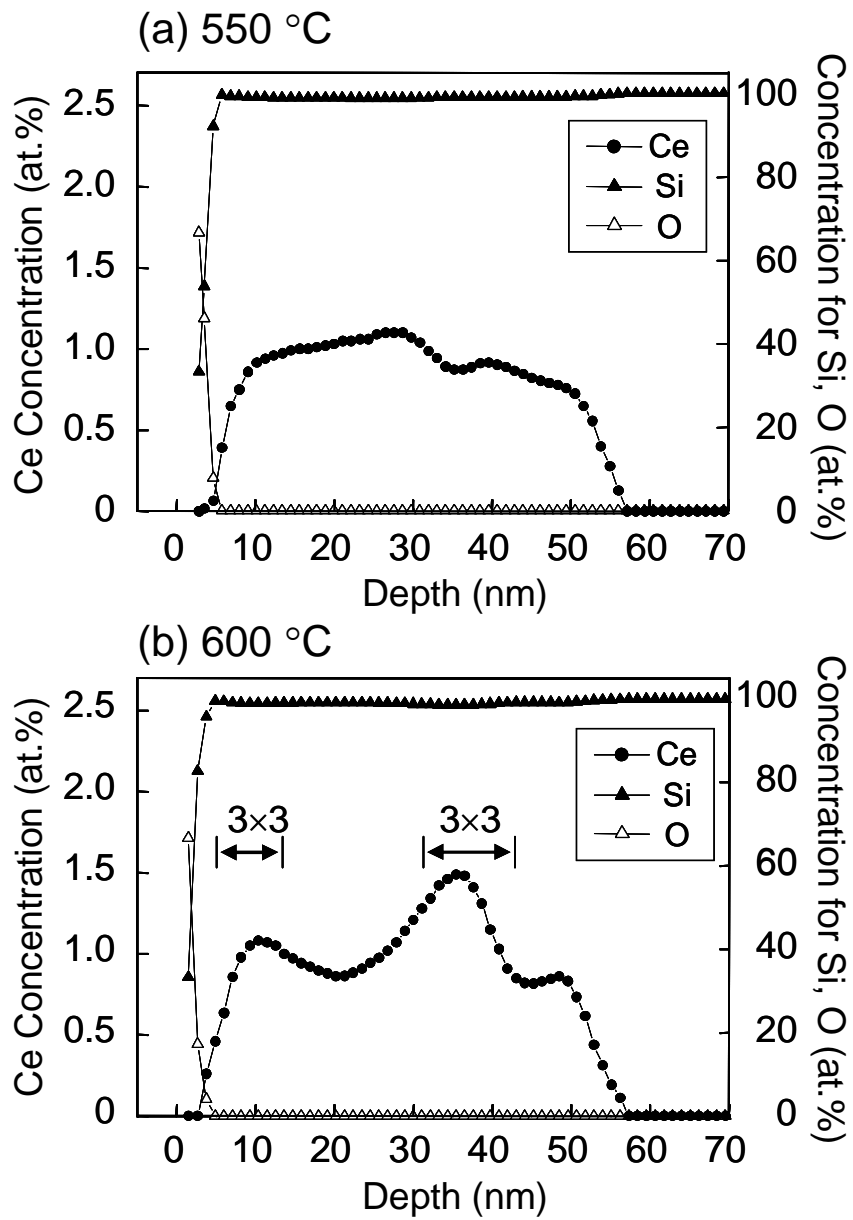Fig. 5-3. HR-RBS spectrum of Si:Ce thin films grown at 550 °C (dot-line) and 600 °C (line).

Fig. 5-4. Depth profile of Ce, Si and O in the Si film doped with 1.1 at.% Ce, deposited at 550 °C (a) and 600 °C (b) measured by HR-RBS. Arrows in (b) indicate where the reconstructed 3×3 surface structure appeared.

5.4 Conclusion

We have examined the surface structure of Si:Ce thin films by *in situ* RHEED analysis. A clear reconstructed 3× surface structure induced by Ce atoms on Si(001) was observed in the films doped with 1.1 at.% and higher. To our knowledge, this is the first report of Ce-induced reconstruction on Si(001). As the Ce concentration was increased, the 3× surface appeared at thinner film thickness. The 3× surface structure requires a certain amount of Ce atoms to form the structure, as well as sufficient heating and incubation time. HR-RBS analysis revealed the variation in the distribution of Ce atoms in the film in association with emergence of the 3× surface. This reconstructed 3× surface structure is thought to be caused by diffusion of Ce atoms to the surface during the deposition, probably due to stress relaxation originating from the difference of the covalent radius of Ce and the Si, and the structure is considered to be in a quasi-stable state. This 3× surface can realize to make the high Ce concentration region on the Si:Ce film surface because of the three-fold periodic atomic arrangement and should be available as a new technique to obtain a diluted magnetic semiconductor with high magnetic element.

References

[1] F. P. Netzer: J. Phys.: Codes. Matter. **7** (1995) 991.

[2] J. Osgaard, M. Christiansen, F. Ørskov, P.J. Godowski : Surf. Sci. **247** (1991) 208.

[3] M. Kuzmin, R. E. Perälä, R.-L. Vaara, A. Mittsev, I.J. Väyrynen : Appl. Surf. Sci. **222** (2004) 394.

[4] M.V. Katkov, J. Nogami: Surf. Sci. **524** (2003) 129.

[5] C. Ohbuchi, J. Nogami: Phys. Rev. B. **66** (2002) 165323.

[6] B. Z. Liu, J. Nogami: Surf. Sci. **540** (2003) 136.

[7] J. Yang, Q. Cai, X.-D. Wang, R. Koch: Surf. Sci. **526** (2003) 219.

[8] Q. Cai, J. Yang, Y. Fu, Y. Wang: Appl. Surf. Sci. **190** (2002) 157.

[9] K. Murata, Y. Yasutake, K Nittoh, K. Sakamoto, S. Fukatsu, and K. Miki: Appl. Phys. Express **3** (2010) 061302.

[10] F. U. Hilebrecht: Appl. Phys. Lett. **55** (1989) 277.

[11] Dohyun Lee, S. M. Jeon, G. Lee, S. Kim, Chanyong Hwang, and Hangil Lee: Surf. Sci. **601** (2007) 3823.

[12] S. S. Iyer, J. C. Tsang, M. W. Copel, P. R. Pukite, and R. M. Tromp: Appl. Phys. Lett. **54** (1989) 219.

[13] P. C. Zalm, G. F. A. van de Walle, D. J. Gravesteijn, and A. A. Van Gorkum: Appl. Phys. Lett. **55** (1989) 2520.

[14] K. Yaji, Y. Ohtsubo, S. Hatta, H. Okuyama, K. Miyamoto, T. Okuda, A. Kimura, H. Namatame, M. Taniguchi, and T. Aruga: Nat. Commun: **1** (2010) 17.

6
Summary

This thesis has been devoted to study the magnetic and electronic properties of diluted magnetic semiconductor Si:Ce films. The objectives were to investigate the Ce-related energy level in the Si band gap of low temperature grown (LT-grown) film and to evaluate the relationship between the energy level and the magnetism. The main result of this work can be summarized as follows.

In chapter 2, the change of carrier type and carrier density associated with Ce incorporation and the Ce-related energy level of LT-grown Si:Ce were investigated. From the Hall effect measurement, parallel conduction with the film and the substrate was observed. Because of the parallel conduction, the evaluation of energy level from the transport was difficult. Using a capacitance-voltage measurements of Si:Ce MIS capacitors, the effect of Ce incorporation was evaluated. In the low Ce concentration, electron density increase with increasing Ce concentration. The electrons probably arise from Si vacancies emission accompanied with Ce incorporation. Additional Ce-doping into Si causes the films to be high resistive. It is indicated that deep level traps increase with Ce increasing from the analysis of $C\text{-}f$ and $G_P/\omega\text{-}f$ measurement. Carrier compensation by the deep level traps causes high resistivity of Si:Ce film. From the XRD measurements, decrease of lattice parameter was observed in the high resistive samples. A high concentration of vacancies would result in formation of vacancy-vacancy and vacancy-Ce complexes. The appearance of deep level traps is

attributed to the presence of these point-defect complexes. The samples with high resistivity show ferromagnetic M-H curve which deteriorate with time and antiferromagnetic or diamagnetic M-H curve.

In chapter 3, LT-grown p-type Si:Ce thin films were fabricated by means of acceptor doping without segregation of Ce silicide. The heavily acceptor doping to the ferromagnetic Si:Ce weaken the ferromagnetic behavior and the films show paramagnetic magnetization behavior. It is suggested that Ce ion is uniformly distributed and no high concentration region of Ce^{3+} ion is included. From the change of the magnetic properties, it is considered that Ce 4f levels lie in the Si band gap near the valence band edge. The film with metallic conduction shows distinct carrier-4f spin exchange interaction by analyzing the MR behavior. The p-f exchange interaction energy of the film is calculated as 52 meV (Al doped Si:Ce) and 48 meV (B doped Si:Ce), respectively. On the basis of this result, the hole plays an important role in the magnetic properties of the Ce-doped Si thin films. In addition to the hole - 4f spin interaction, it is also important for the ferromagnetism in Si:Ce that Fermi level lies in the Ce 4f states in the band gap..

In chapter 4, Si:2.9 at.%Ce film was successfully grown without silicide precipitation on epitaxial grown ferroelectric $YMnO_3$ though it was a polycrystalline film. The dielectric properties of bottom gate type Pt/$YMnO_3$/Si:2.9at%Ce/Al MFS structure were investigated for the application for a electric field effect study. Although the capacitance shows frequency dispersion, the capacitor exhibits a ferroelectric type C-V hysteresis loop. Detailed dielectric analysis revealed that the C-V hysteresis was caused by both ferroelectricity and space charge. From the P-V measurements at 100 kHz, the measured polarization value originated from ferroelectric $YMnO_3$ was enough

to obtain the carrier inversion of Si though ferroelectric behaviors such as remnant polarization and saturation of polarization were not recognized,.

In chapter 5, the surface structure of Si:Ce thin films were investigated by *in situ* RHEED analysis for the candidate of novel Ce doping method. A clear reconstructed 3× surface structure induced by Ce atoms on Si(001) was observed in the films doped above 1.1 at.%. To our knowledge, this is the first report of Ce-induced reconstruction on Si(001). As the Ce concentration was increased, the 3× surface appeared at thinner film thickness. The 3× surface structure requires a certain amount of Ce atoms to form the structure, as well as sufficient heating and incubation time. HR-RBS analysis revealed the variation in the distribution of Ce atoms in the film in association with emergence of the 3× surface. This reconstructed 3× surface structure is thought to be caused by diffusion of Ce atoms to the surface during the deposition, probably due to stress relaxation originating from the difference of the covalent radius of Ce and the Si, and the structure is considered to be in a quasi-stable state. Some of the films in which the 3× surface structure is observed show ferromagnetic magnetization behavior. This reconstructed surface with high Ce concentration should be available as a new technique to obtain a Si:Ce with high Ce concentration.

Based on these results, the author propose a mechanism of ferromagnetism in Si:Ce film here. It is expected that the 4*f* orbitals of Ce hybridize with valence orbitals. As a result, Ce 4*f* levels lie near the edge of the valence band by increasing the Coulomb interaction between 4*f* and external electrons. From the results of the chapter 2, existence of the midgap states derived from complex defects is indicated on the LT-grown Si:Ce films. From the results of the chapter 3, it is indicated that ferromagnetic behavior in the LT-grown Si:Ce is suppressed by heavily doping of the

shallow acceptor though it has the *p-f* exchange interaction. Based on these results, it is considered that the LT-grown Si:Ce have the energy band diagram as shown in Fig. 6-1. The 4*f* levels lie in the Si band gap. If the 4*f* levels lie deep in the valence band, *p-f* exchange Zener model will be considered as the main origin of the ferromagnetism. According to the *p-f* exchange Zener model, it is expected that acceptor doping enhance the ferromagnetic nature of the Si:Ce films. In fact, however, ferromagnetic behavior was suppressed by the acceptor doping. This experimental result contradicts the *p-f* exchange Zener model. The energy band picture as shown in Fig. 6-1, which is the double-exchange interaction model rather than *p-f* exchange Zener model, can well explain the experimental results. In the high Ce concentration region as shown in Fig. 6-2, the hopping conduction between the localized states will occur with the carrier transport in the valence band or conduction band. It is possible that the double exchange interaction acts by the hopping conduction between 4*f* states of adjacent Ce ions. The 3× surface reconstruction induced by Ce atom can realize to make the high Ce concentration region on the Si:Ce film surface. Although there is no direct evidence that the origin of ferromagnetism in Si:Ce is the double exchange interaction, this mechanism can explain well the experimental results. In either way, *p-f* exchange interaction is shown and it is expected that a control of the magnetic properties by the external field such as electric field and light.

The author eventually concludes that the origin of the ferromagnetism in Si:Ce films is expected to be the double exchange interaction mediated by *p-f* exchange interaction. The Ce^{3+} state in high Ce concentration region and the Fermi level position lying in the 4f states are responsible for the ferromagnetic behavior in Ce-doped Si films.
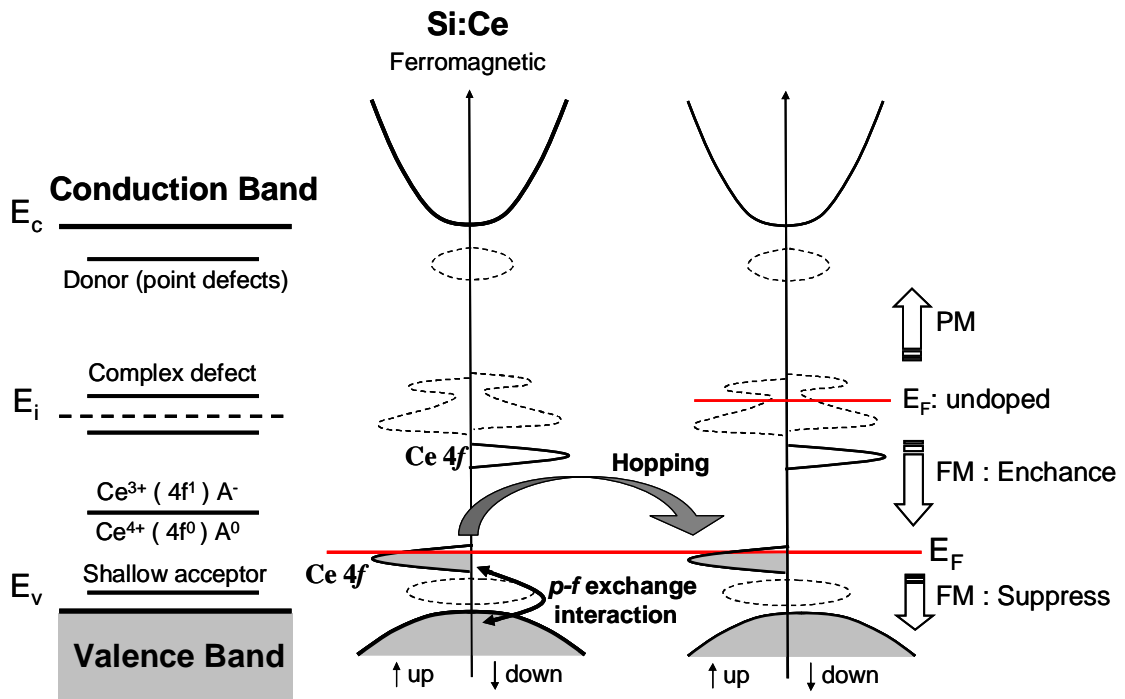
Fig. 6-1.   A mechanism of ferromagnetism in Si:Ce and illustration diagram
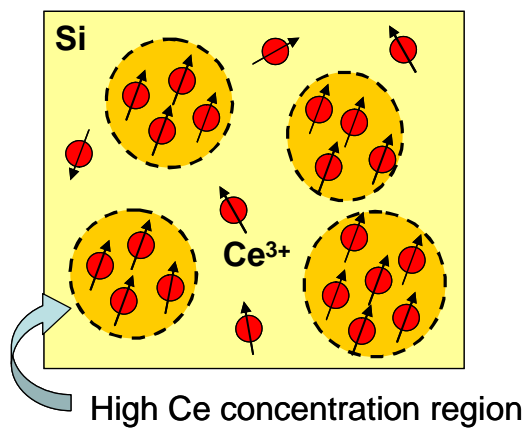of the change of the magnetic property

Fig. 6-2.   A schematic illustration of magnetic structure in Si:Ce films

Acknowledgments

Original Articles Regarding This Thesis

No.	Title	Authors	Journal	Related Section
1	Evaluation of Ce doped Si thin films using MIS structure	D. Shindo T. Yoshimura N. Fujimura	Journal of Applied Physics, submitted.	Chapter 2
2	The effects of aluminum doping for the magnetotransport property of Si:Ce thin films	D. Shindo K. Fujii T. Terao S. Sakurai S. Mori K. Kurushima N. Fujimura	Journal of Applied Physics, Vol. 107, 09C308 (2010). Total 3 pages	Chapter 3
3	Dielectric properties of ferroelectric/DMS heterointerface using $YMnO_3$ and Ce doped Si	D. Shindo T. Yoshimura N. Fujimura	Applied Surface Science, Vol. 254, pp.6218-6221, (2008).	Chapter 4
4	Ce-induced reconstructions on Si(001) surface	D. Shindo S. Sakurai N. Fujimura	Japanese Journal of Applied Physics, submitted.	Chapter 5